Open access • Journal Article • DOI:10.1016/J.COSSMS.2015.08.001

Critical properties of Cu6Sn5 in electronic devices: Recent progress and a review

Mu Dekui, Mu Dekui, Stuart McDonald, J. Read ...+2 more authors

Institutions: Huaqiao University, University of Queensland

Published on: 01 Apr 2016 - Current Opinion in Solid State & Materials Science (Elsevier Limited)

Topics: Ball grid array

Critical properties of Cu_6Sn_5 in electronic devices: Recent progress and a review

D. Mu[1, 2, 3, 4], S. D. McDonald[2, 3], J. Read[2, 3], H. Huang[3], K. Nogita[2, 3]*

[1] Institute of Manufacturing Engineering, Huaqiao University, Xiamen 361021, China

[2] Nihon Superior Centre for the Manufacture of Electronic Materials (NS CMEM), [3] School of Mechanical and Mining Engineering, The University of Queensland, Brisbane, Queensland 4072, Australia

[4] NihonSuperior Co., Ltd., Osaka 564-0063, Japan

*k.nogita@uq.edu.au; Tel.: +61 7 3365 3919; Fax: +61 7 3365 3888

Abstract

As the most common of the intermetallic compounds (IMCs) formed between Sn base solders and Cu substrates during the packaging of integrated circuits (ICs), Cu_6Sn_5 is frequently involved in the fabrication of solder joints and plays an important role in the integrity of electronic devices. This is especially true for recently developed micro-bumps in 3-dimensional (3D) high-density integrated circuits (ICs), in which the volume fraction of Cu_6Sn_5 is significantly higher than in conventional ball grid array (BGA) or through hole pin (THP) arrangements. Recently, with the use of advanced characterization techniques, significant progress has been made in the understanding of Cu_6Sn_5 intermetallics in terms of their crystal structure, solidification behaviour, role in interface reactions, thermal expansion and mechanical properties. This improved understanding is of fundamental importance for the production of next generation electronic devices, however there is no existing comprehensive summary of this research available. Here, we provide a review on the properties of Cu_6Sn_5 with a focus on: 1) identification of crystal structure and possible phase transformations of Cu_6Sn_5 in real solder joints; 2) formation of Cu_6Sn_5 during solidification of commonly used Pb-free alloys and its influence on the final microstructure; 3) the formation and growth texture of interfacial Cu_6Sn_5; 4) thermal expansion and mechanical properties of Cu_6Sn_5 and the relationship between crystal structure and temperature. The effects of selected alloying elements that have remarkable influences on the above properties are also discussed. The aim of this paper is to identify the key factors that affect the properties of this important IMC and the relationship between these properties and the integrity of solder joints under various conditions.

Key words: soldering, Cu_6Sn_5, crystal structure, phase transformation, solidification, thermo-mechanical properties

1. Introduction

Recently, there has been an increase in research activity in the field of miniaturising electronic devices. This increase is due to the change to three-dimensional integrated circuitry (3D IC) in the microelectronics industry in attempts to overcome the speed limitations imposed by two-dimensional circuitry [1-3]. In addition to the recent popularity of portable microelectronic devices, database storage advances driven by "Cloud computing" initiatives are accelerating the rate of miniaturisation allowing "Moore's law" [2, 3] to be satisfied. This change in circuit architecture from 2D to 3D is occurring at the same time that industry is still adapting to the use of Pb-free solder technology. The removal of Pb from conventional solders in electronic equipment was mandated in the European Union (EU) in 2006 and other markets, including Japan, China and California, are affected by this and similar legislation. As a result, alternative (Pb-free) solder systems (e.g.,Sn-Ag, Sn-Bi, Sn-Zn, Sn-Cu and Sn-Ag-Cu) have been developed [4-7], but uncertainties relating to reliability, have limited these alloys to use in consumers products, with exemptions for military, medical and other specialised applications. While industry is coming to terms with the use of Pb-free solder in 2D ICs, more research is required to make the transition to 3D manufacturing techniques.

The 'anatomy' of a soldered electrical connection in modern electronic devices consists not only of the metallic substrate and solder, but also the interfacial area, which is critical for imparting suitable mechanical and electrical properties. This interfacial area contains reaction products that form through a combination of solidification and diffusion, during, and after, the manufacturing process. The reaction products are typically the intermetallic compounds (IMCs) of Cu_6Sn_5 and Cu_3Sn, often of complex crystal structures and including trace elements from both the substrate and the solder. There has been a simultaneous increase in the complexity and spatial density of electrical packages (combined circuitry/chips/solder etc.,) during the current period of transition from traditional to Pb-free soldering. This miniaturisation of circuitry has resulted in proportionally smaller volumes of solder at the electrical interconnects. As such, there has been a relative increase in the volume fraction of IMCs in the microstructure of solder joints and in some cases, a

solder joint may consist almost entirely of IMCs with a single or at most a few unique crystallographic grains [1-3, 8]. This is particularly important since single grain IMCs that are present in micro-circuitry will behave differently than larger multi-grained IMCs found in more conventional solder joints. Therefore, the current understanding of the 'bulk' properties of intermetallics (which is already limited for many alloy/substrate combinations) is not always relevant when designing high performance 3D IC electrical packages. For this reason, it is essential to understand the crystallography, morphology and anisotropic thermo-mechanical properties of Cu_6Sn_5 intermetallics and the impact these have on the integrity of solder joints for micro-electronics applications.

During past decades, the properties of Cu_6Sn_5 have been extensively investigated [9-16] and significant progress has been made with the help of advanced characterization techniques. However, these results had never been well summarized in the literature. This paper therefore aims to provide a focused review on the properties of Cu_6Sn_5 such as crystal structure, solidification behaviour, interfacial formation, and thermo-mechanical properties.

2. Crystal structure and phase transformation

It is well known that the phase transformation of Cu_6Sn_5 during the service of electronic devices has a significant effect on the mechanical strength of solder joints. As a result, the knowledge on the crystal structure and phase transformation is essential to understanding the properties of Cu_6Sn_5 intermetallics, and hence the reliability of solder joints. However, this important knowledge has never been well summarised before.

2.1 Crystal structure

In the Sn-Cu phase diagram as shown in Fig. 1 [17], Cu_6Sn_5 has at least two crystal structures in the solid state, as shown in Fig. 2 (a) and (b): the η' monoclinic phase is stable at temperatures below 186 ^oC and the η hexagonal phase is stable at temperatures above 186 ^oC [18]. The η'-Cu_6Sn_5 is of a C2/c space group and the η-Cu_6Sn_5 is of a $P6_3/mmc$ space group, respectively [17]. The composition regions of both η' and η-Cu_6Sn_5 are narrow bands rather than lines, and the η-Cu_6Sn_5 phase field is skewed towards the Cu-rich side as the

temperature increases. The hexagonal Cu_6Sn_5 has a NiAs-type structure ($B8_1$-structure), with alternating close-packed layers of Sn and Cu atoms [19]. For the high-temperature η phase stable at temperatures above 186 ^oC, Larsson et al. identified two superstructures as η^6 and η^8, which are slightly more Cu-rich (55.56 at.%) compared to Cu_6Sn_5 (54.50 at.%) [9]. The η^6 structure is stable at temperatures above 350^oC and is of a C2 space group; while η^8 is stable at temperatures from 350 to 186 ^oC and is of a P21/c space group [20]. Recently, a new long-ordered monoclinic η^{4+1} phase was found to form in a high-purity stoichiometric sample [21]. This newly indexed η^{4+1} Cu_6Sn_5 is stable at temperature below 210 ^oC and can be represented by the periodic stacking of four η^8 units plus one η' unit of Cu_6Sn_5 [21]. The η^{4+1} Cu_6Sn_5 is a Cu-rich phase compared to η'-Cu_6Sn_5. As shown in Fig. 2 [18], the surplus Cu atoms occupy the tetrahedral interstices in the η-Cu_6Sn_5 unit cell, which results in the difference in crystal structures of η-Cu_6Sn_5. The lattice parameters of monoclinic and hexagonal Cu_6Sn_5 phases have been summarised in Table 1. It should be noted that, the hexagonal Cu_6Sn_5 is of a faceted hexagonal structure with the a-axis longer than the c-axis.

2.2 Phase transformation and stabilization

In the literature, the η-η' transformation of Cu_6Sn_5 at the equilibrium temperature of 186 ^oC has attracted significant research attention [15, 22-25]. This phase transformation used to be considered as an order-disorder transition [15, 22-24]. However, the morphology coarsening induced by the η-η' transformation of single-crystalline Cu_6Sn_5 and subsequent differential scanning calorimetry (DSC) analysis indicated a polymorphic transition mechanism [25]. The kinetics of this polymorphic η-η' transformation of Cu_6Sn_5 at temperatures below 186 ^oC were recently obtained by synchrotron [18, 26] and laboratory [27] X-ray diffraction techniques. According to the time-temperature-transformation (TTT) curves given in Fig. 3 [18], the monoclinic η'-Cu_6Sn_5 starts to transform into the hexagonal structure in approximately 100 seconds at temperatures around 150^oC [26, 27]; while laboratory based X-ray diffraction gives a much slower transformation kinetic, which is most likely due to the longer time necessary to identify the monoclinic peaks. Using DSC and synchrotron X-ray diffraction under continuous and isothermal cooling conditions, the polymorphic transformation temperature of the η^{4+1} phase was confirmed as 208 ^oC and the transformation kinetics are faster than that of the η phase as shown in Fig. 3 [18]. The hexagonal to monoclinic transformation was activated within less than 100 seconds. At room temperature, the

polymorphic transformation of the η and η^{4+1} phase is sluggish and is unlikely to occur in any reasonable timeframe.

According to room temperature density data, the η-η' transformation of Cu_6Sn_5 results in a 2.15% volume expansion [15], which leads to undesirable internal stresses in the IMC layer. Using TEM, see Fig. 4, and DSC techniques, Nogita and Nishimura firstly reported that the addition of 9 at% Ni stabilizes the as-cast hexagonal η-Cu_6Sn_5 at room temperature [28]. The addition of 0.05Ni (in wt% unless mentioned elsewhere) in a Sn0.7Cu/Cu reaction couple was also reported to stabilize the interfacial Cu_6Sn_5 which has a Ni content of approximately 4.8 at% [29]. Recently, the minimum Ni concentration necessary for stabilization of high-purity stoichiometric Cu_6Sn_5 was found to be 1 at% using step heating synchrotron X-ray diffraction [30]. Because of the sluggish kinetics at the very Sn-rich corner of the Sn-Cu-Ni system [31], the stable crystal structure of $(Cu,Ni)_6Sn_5$ is yet to be confirmed experimentally. By first principle calculation, Yu et al. reported the stable phase of $(Cu,Ni)_6Sn_5$ as $Cu_4Ni_2Sn_5$ with a nominal Ni content of around 13.3wt% [32]. Schwingenschlögl et al. found that, at T = 0 K, the monoclinic η'-Cu_6Sn_5 phase has a lower total energy of 1.21eV per two formula units than hexagonal η-Cu_6Sn_5 [29]. The addition of 5 at% Ni reduces the total energy difference to 0.90eV per two formula units at T = 0 K, and subsequently stabilizes the meta-stable hexagonal structure at temperatures below 186°C [29].

Besides Ni, additions of 0.8-2.1 at% of Zn were also reported to stabilize the hexagonal η-Cu_6Sn_5 after aging at 150°C for 5 days [33]. A first principle calculation revealed that Zn atoms preferentially occupy the Sn1C site unit cell and the hybridization between Zn-d and Sn-s states stabilizes meta-stable hexagonal phases [34]. Moreover, monoclinic Cu_6ZnSn_4 with Sn3 (4e) sites occupied by Zn atoms was found to be the most stable phase [35]. Recently, Zeng et al. systematically investigated the stabilization effects of Zn, Au and In on stoichiometric Cu_6Sn_5 prepared by direct casting [36]. It was found that the addition of 2wt% Au or Zn completely stabilizes the as-cast η-Cu_6Sn_5 at room temperature; while an 8wt% addition of In is necessary to stabilize hexagonal η-Cu_6Sn_5 after casting [36]. Therefore, the In-induced stabilization is kinetic, similar to the stabilization effect of Sb, which reduces the diffusivity of Cu and impedes the twinning of η-Cu_6Sn_5

[37]. The effects of doping with Zn, Au and In on the stabilization of the newly indexed monoclinic η^{4+1} phase of Cu_6Sn_5 were also studied at temperatures between -80 ^oC to 240 ^oC [38]. Along with the strong stabilization effects of Ni, Au and Zn, a partial stabilization effect of In was observed for the η^{4+1} Cu_6Sn_5 phase [38] and In reduced the initial transformation temperature and transformation rate under both continuous and isothermal cooling. Moreover, it was found that the Zn and In substitute Sn atoms, while Au substitutes for the Cu atoms in the monoclinic η^{4+1} Cu_6Sn_5 unit cell [38]. Using partial density of state simulation, the hybridization between Zn-d and Sn-s states, Au-d and Cu-d states, In-s and Sn-s was found to be responsible for the stabilization of η-Cu_6Sn_5 doped with Zn, Au and In, respectively [38]. In summary, these computational works suggested the substituting atoms stabilize the hexagonal structure by the formation of new bonds with Sn or Cu atoms in the Cu_6Sn_5 unit cell [29, 32, 34, 35, 38].

3. Solidification in Sn-based alloys

SnPb alloys consist of Sn and Pb phases and are free from the formation of intermetallics. A major difference between SnPb solders and Sn-based Pb-free solders is the formation of IMCs during solidification. Because of the small volume fraction of IMCs (less than 5% in most cases) involved, these IMCs generally solidify with a faceted morphology, and if the composition is such that the IMC precedes Sn formation in the solidification sequence, these particles have the potential to act as nuclei for Sn grains and hence affect the microstructure and mechanical properties of solder alloys.

3.1 Solidification in the Sn-Cu system

Near-eutectic Sn-Cu based solders are commonly used for wave soldering and hence their solidification behaviour has attracted extensive research attention. In the literature, the composition of the Sn-rich eutectic reaction has been reported at Sn-0.7Cu [4, 5, 31] and Sn-0.9Cu [39, 40]. Drevet et al. reported a regular non-faceted-faceted solidification of eutectic Sn-Cu alloys (0.83 to 0.9 Cu), in which Cu_6Sn_5 fibres grow perpendicular to the basal (001) plane and control the growth of Sn in the eutectic [11]. In a recent study, the eutectic point of the Sn-Cu system was confirmed to be Sn-0.9Cu, as indicated by the microstructure of directionally solidified Sn-Cu alloys in Fig. 5 [41],. Moreover, the skewed coupled zone also suggests a weakly irregular solidification of near-eutectic Sn-0.5/0.7Cu alloys [41]. By *in-situ* observation of a hypo-

eutectic Sn-0.7Cu alloy [42], Cu_6Sn_5 was found to nucleate first in Sn-Cu_6Sn_5 eutectic and the preferential growth of Cu_6Sn_5 dominated eutectic growth.

Recently, directional solidification studies on the hyper-eutectic side of the Sn-Cu system have been reported [43-45]. A rod eutectic with Cu_6Sn_5 as the leading phase was reported for Sn-1.2Cu alloys cooled at temperature gradients from 2.69 to 8.88 K/mm and pulling speeds from 2.78 to 136.36 μm/s [43]. In contrast, at a temperature gradient of approximately 1.1 K/mm and pulling speeds from 15 to $3 \cdot 10^6$ μm/s, the growth of primary Cu_6Sn_5 in Sn-1.2Cu was found to be irregular with non-uniform spaces between Cu_6Sn_5 rods [44]. A Cu concentration gradient was observed along the samples cooled in a vertical Bridgman furnace, but the Cu content of Cu_6Sn_5 was constant as 53.5 at% [44]. By further increasing the Cu content [45], the chemical analysis of directionally solidified Sn-2/2.8Cu alloys showed that the Cu gradient is mostly established at the surface of the sample, but the Cu content of Cu_6Sn_5 is only slightly different along the cooling direction. Moreover, Cu_3Sn was also detected in a Sn-2.8Cu alloy [45]. According to the above solidification studies, Cu_6Sn_5 is the leading phase during eutectic solidification of near-eutectic Sn-Cu solders. On the hyper-eutectic side, Cu_6Sn_5 is the primary phase. Fig. 6 shows the air cooled microstructure of Sn-0.3/0.6/1.3/1.7Cu alloys [46]. Sn dendrites and eutectic were observed for all compositions and primary Cu_6Sn_5 particles were observed in Sn-1.3/1.7Cu alloys. As the Cu content increased, the Sn dendrites became finer [46].

3.1.2 Effect of selected alloying elements

Sn-Cu alloys have disadvantages such as poor wettability, high melting temperatures relative to traditional alloys and low resistance to thermal fatigue. Therefore, a number of alloying elements are used to improve the solderability of Sn-Cu alloys. In particular, alloying elements such as Ni, Zn and rare earths (RE) have demonstrated remarkable effects on the solidification of Sn-Cu alloys [47]. Among these alloying elements, ppm level additions of Ni are reported to improve flow characteristics of Sn-0.7Cu alloys [48, 49] and result in an increase in the amount of eutectic microstructure of Sn-0.7Cu alloys [50], as shown in Fig. 7. As the Ni content increases, the Cu_6Sn_5 phase becomes more rounded and the volume fraction of Sn-dendrites clearly decreases [50]. The Ni-induced improvement on the microstructure and fluidity of Sn-0.7Cu is associated

with the Ni-induced eutectic-like solidification of Sn-Cu alloys and has been confirmed through directional solidification of Sn-0.7Cu with trace amounts of Ni addition [48, 51]. Moreover, directional solidification studies of Sn-0.7Cu-Ni alloys suggested the eutectic valley in the Sn-rich side of Sn-Cu-Ni phase diagram is close to Sn-0.7Cu-0.05Ni [52], which explains how Ni improves the fluidity of a Sn-0.7Cu alloy.

In addition to Ni, 0.2wt% Zn was reported to refine the β-Sn grains in the Sn-0.7Cu alloys [53]. However, a further increase of Zn content prevented the formation of Cu_6Sn_5 and led to the formation of a dispersed Cu-Zn phase [53], because Zn is highly active and reacts readily with Cu [54]. Detailed solidification data at the Sn-rich side of the Sn-Cu-Zn system is not available in the literature and the role of Zn in the solidification of near-eutectic Sn-Cu alloys is not fully understood yet. However, according to our recent directional solidification and synchrotron *in-situ* observation of the solidification of Sn-0.7Cu-0.15Zn alloy [55], Zn and Cu solutes which is rejected from the advancing β-Sn/liquid interface led to constitutional supercooling, which therefore affects the growth of Sn dendrites [55]. In addition, the unevenly distributed Zn also leads to the formation of CuZn IMCs after the freezing of the β-Sn and eutectic [55].

The addition of 0.5wt% RE (Ce and La) to Sn-0.7Cu alloy was found to refine the grain size of β-Sn and resulted in a uniform distribution of Cu_6Sn_5 [56]. The addition of 0.4wt%Co in Sn-0.7Cu alloy also results in the fine dispersion of $(Cu, Co)_6Sn_5$ and the formation of a new $(Cu, Co)Sn_2$ phase [57]; while the addition of 0.15 and 0.45wt% Co has been found to enhance the nucleation of Cu_6Sn_5 in Sn-Ag-Cu alloys [58]. As the use of high-Pb high temperature solders will be banned in near future, there is an urgent demand for alternative high-temperature Pb-free solders in the electronics industry [59, 60]. Hyper-eutectic Sn-Cu alloys have been proposed for high-temperature soldering applications such as motor litz [61], but suffer from the formation of massive IMCs [60]. It has been found that trace additions of Al (250 ppm) to the Sn-4Cu alloy significantly refines the Cu_6Sn_5 grains as shown in Fig. 8 [62], while the addition of Ni, Ge, Ag and Pb resulted in no reduction in grain size of Cu_6Sn_5. Further study has revealed that the addition of 0.02-0.2wt% Al can refine the Cu_6Sn_5 by heterogeneous nucleation and constitutional supercooling ahead of Cu_6Sn_5

crystals [63]. In principle, these alloying elements refine the microstructure of Sn-Cu alloys by either modifying the solidification of the base alloy or enhancing the nucleation of Cu_6Sn_5 IMCs.

3.2 Solidification in Sn-Ag-Cu system

In SnAgCu solder alloys, Cu_6Sn_5 solidifies as the faceted phase, with a grain size much bigger than Ag_3Sn. As a result, Cu_6Sn_5 has less effect on improving the mechanical properties of the solder. The dislocation bowing induced by Ag_3Sn was reported to be the origin of improved solder strength of Sn-Ag-Cu alloys with Ag contents from 0 to 5 wt%. [64, 65]. Due to its excellent mechanical properties, the Sn-Ag-Cu family of solders is commonly used for reflow soldering. Despite earlier disagreement [66], the eutectic point of Sn-Ag-Cu was confirmed as Sn-3.5Ag-0.9Cu [67, 68]. During the solidification of the eutectic Sn-Ag-Cu alloy, both Ag_3Sn and Cu_6Sn_5 form during the ternary eutectic reaction of $L \rightarrow Sn+Ag_3Sn+Cu_6Sn_5$ [68]. Both Ag_3Sn and Cu_6Sn_5 are faceted phases and the Cu_6Sn_5 is likely to be the leading phase [68]. When the composition is slightly off-eutectic (Sn-3.8Ag-0.7Cu), the Ag_3Sn will be the leading phase due to the change of solidification reaction [69]. In practice, several near-eutectic Sn-Ag-Cu alloys were proposed for reflow soldering; however, compared to Sn-Cu alloys, the solidification path of these near-eutectic Sn-Ag-Cu solders has not been comprehensively studied. The solid state coarsening of Ag_3Sn and Cu_6Sn_5 (in both Sn-Cu and Sn-Ag-Cu systems) is controlled by the diffusion of Sn and Cu, respectively [70, 71]. However, the coarsening speed of Cu_6Sn_5 is significantly faster than that of Ag_3Sn, 50% Cu atoms will concentrate as large Cu_6Sn_5 particles after 100 hour aging of the Sn-3.8Ag-0.7Cu alloy at 150 ^oC [72].

3.2.1 Effect of selected alloying elements

During the solidification of near-eutectic Sn-Ag-Cu alloys, the microstructure that develops often consists of large Sn grains [73], which are commonly considered a determinant of the integrity of solder joints because of the highly anisotropic properties of the body centred tetragonal structure of Sn [74]. This is particularly true for the recently developed low-Ag Sn-Ag-Cu alloys with Ag content equal or less than 1 wt%. A large number of alloying elements, including rare earth element and the metals Sb, Ti, Mn, Zn, In and Ni, were added to either near-eutectic or low-Ag Sn-Ag-Cu alloys [75, 76]. However, most of these elements, except

Ni, refine the microstructure of Sn-Ag-Cu alloys by formation of new IMCs other than Cu_6Sn_5 [76]. There is limited research available on methods of controlling the Sn grain size in these alloys.

4. Interfacial microstructure formation

The interface reaction is essential to bond the solder and substrate metals. Periodic reviews of the effects of alloying elements on the interfacial formation of Cu_6Sn_5 are available in literature [77, 78], here, we firstly focus on the physics of Cu_6Sn_5 formation during different reaction stages, from the initial wetting to an extended reaction such as the transient liquid phase reaction. Then, Cu_6Sn_5 formation in common solder systems is also discussed, with particular attention given to the formation morphology and growth texture of interfacial Cu_6Sn_5 subject to the effects of alloying elements. To finish this section, the formation of Cu_6Sn_5 in micro-bumps in 3D ICs is studied.

4.1 In 2 dimensional arrangement

4.1.1 General formation sequence on polycrystalline Cu

Cu is the most commonly used under bump metallization (UBM) material because of its superior thermal and electrical conductivities. As a result, the formation of Cu_6Sn_5 on a Cu substrate has attracted the most research attention. During the initial stage of the interface reaction between liquid Sn and solid Cu, the thermodynamically preferential formation of Cu_6Sn_5 over Cu_3Sn can be observed from the calculated Gibbs free energy and the driving force for formation in the Sn-Cu system at the Sn-rich side, as given in Fig. 9 [79]. As suggested by the negative Gibbs free energy, the formation of Cu_3Sn is also thermodynamically possible once the interface between Cu and Cu_6Sn_5 forms [79]. Experimentally, Cu_6Sn_5 has been confirmed as the first phase that precipitates at the liquid Sn and solid Cu interface at temperatures between 240 °C and 300 °C [14]. It was found that the Cu substrate surface was covered with Cu_6Sn_5 crystallites one second after dipping a Cu strip into molten pure Sn. Other experimental work has reported that the Cu_6Sn_5 crystallites have covered the Cu surface within several milliseconds [80]. Park et al. proposed that the lower the interface energy between liquid and IMCs; the easier it is for Cu_6Sn_5 to nucleate. As a result, Cu_6Sn_5 is more likely to nucleate at the triple point of the substrate, solder and IMC phase, which is also expected from the modified Young's equation as the lowest interface energy at the wetting edge (α>0 degree) [81]. The precipitated Cu_6Sn_5 grains grow parallel to the solder/substrate interface and the growth in the direction

perpendicular to the solder/substrate interface starts only after the precipitated Cu_6Sn_5 grains intersect each other [81]. As indicated by the experimental results, this early stage nucleation is completed in a few seconds [14, 80, 81].

After early stage nucleation, the Cu_6Sn_5 formed at the interface between pure Sn and Cu substrates coarsens to a faceted scallop-like morphology, see Fig. 10 (a) [82]. The coarsening of Cu_6Sn_5 is a ripening process in which thermally stable grains consume their neighbours that have a higher surface energy. As a result, the anisotropic nature of the hexagonal structure of Cu_6Sn_5 results in the formation of a textured interface. As shown in Fig. 10 (b) [83], A (101) growth texture has been reported for Cu_6Sn_5 formed between Sn and a poly-crystalline Cu substrate at 242 ^oC [83] and 280 ^oC [84]. Gusak and Tu have proposed a non-conservation flux driven ripening (FDR) model to describe the ripening process of Cu_6Sn_5 as driven by the Cu diffusion flux along grain boundaries [13]. The main difference between the non-conservation FDR model and the classical Lifshitz-Slezov-Wagner (LSW) model is that the ripening process is considered as an open system and the incoming Cu flux along the grain boundaries drives the ripening process as:

$$< R >^3 = (0.913)^3 kt \qquad (1)$$

and

$$k = \frac{9}{2}\frac{n}{n_i}\frac{D\,(C^b - C^e)\delta}{C_i} \qquad (2)$$

where: R is the radius of round Cu_6Sn_5 scallops; t is the reaction time; D is the diffusivity constant; δ is the width of grain channel; n is the atomic density or number of atoms per unit volume in the melt or molten solder; n_i is atomic density in IMC's i.e., the number of atoms per unit volume and C_i is atomic fraction of Cu in IMC's, which is 6/11 in Cu_6Sn_5. C^e is the equilibrium atomic concentration of Cu in solder at the planar interface between Cu_6Sn_5 and molten solder, C^b is the equilibrium concentration of Cu in the molten solder at the interface between the substrate and solder at the channel's bottom. For a given reaction system, other parameters except the composition difference of Cu at the bottom and top ends of the grain channel, item $(C^b - C^e)$ in Equation 3, can be approximated as constants at a given moment of the reaction. As a result, it is clear that the composition difference is the only variable and dominates in Eq.(2). In other words, the fast diffusion of Cu flux through the channels between Cu_6Sn_5 grain boundaries controls the ripening of

Cu_6Sn_5 scallops [85]. Indeed, both the non-conservation FDR model and the classic LSW model give a growth exponent of 1/3; however, the non-conservation FDR facilitates the prediction of distribution of Cu_6Sn_5 grain size. Alternatively, Schaefer et al. proposed another model considering solid state grain boundary diffusion growth mechanisms controlling the growth of Cu_6Sn_5 [86]. Schaefer's model uses a similar geometry to the non-conservation FDR model except assuming a hexagonal grain of Cu_6Sn_5. Moreover, it also gives a growth exponent close to 1/3.

Experimentally, a grain boundary channel with a width of approximately one nanometre was observed between Cu_6Sn_5 scallops at the interface between Sn and Cu [85]. Energy Dispersive Spectrometer (EDS) spot analysis at the regions close to the Cu_6Sn_5/Cu_3Sn and Cu_6Sn_5/solder interface also evidenced the existence of the Cu flux from the substrate to the IMC side as shown in Fig. 11 [87]. Moreover, several previous kinetic studies on the interface reaction between liquid Sn and solid Cu also reported the growth exponents of Cu_6Sn_5 close to 1/3 [85, 88-90], indicative of a grain boundary diffusion controlled growth mechanism. In recent computational work, the grain boundary diffusion coefficient of Cu with one order magnitude higher than the diffusion coefficient through Cu_6Sn_5 phase gave a result in good agreement with these experimental results [91]. However, strict assumptions have been made in the FDR model such as hemispherical (equal height and width) Cu_6Sn_5 scallops and no precipitation or dissolution of Cu_6Sn_5 in the molten solder. The former assumption cannot hold when the Cu_6Sn_5 grains elongate as the reaction time extends. Moreover, some kinetic studies have also proposed the separation of Cu flux into the solder alloys must be considered when predicting the size distribution of Cu_6Sn_5 [92], or the reported binary layer structure between pure Sn and Cu, suggesting the precipitation of Cu_6Sn_5 from solder molten should not be neglected [77].

The liquid-solid interface reaction in conventional soldering processes lasts for a period from several seconds to a few minutes (typically less than 10 minutes). However, high-temperature Pb-free soldering applications have led to the development of a transient liquid phase (TLP) reaction technique, which emphasizes the formation of Cu_6Sn_5 during an extended liquid phase reaction [93]. Previous research on the

reactions between a Cu substrate and SnPb, Sn and Sn-based solders reported a stage dependent growth rate of Cu_6Sn_5 [83, 94]. In a recent study [93], the growth of Cu_6Sn_5 was reported to be better described by a grain boundary control growth with time-dependence factor β of the width of grain channels δ, or at least the volume control growth was not obtained. This is in contrast with another study on the reaction between Sn and Cu that asserted volume control growth dominated the growth of Cu_6Sn_5 after 30 minutes of liquid reaction [84]. However, both studies are based on the growth thickness of Cu_6Sn_5 without detailed characterization of interface microstructure [84, 93], which is necessary to estimate the Cu flux through grain boundary diffusion and volume diffusion. In an *in-situ* observation of Cu_6Sn_5 growth between pure Sn and Cu transient liquid phase interface with reaction times up to 4350 seconds, the ratio between the width and height of Cu_6Sn_5 grains that consumes it neighbours is close to 2 [95], and the plot of the width and height of Cu_6Sn_5 grains also suggest that the ripening of Cu_6Sn_5 remains in a stable stage without significant changes of the ratio between the height and width of Cu_6Sn_5 grains [95], which suggest a constant growth mechanism during the extended liquid reaction period.

Another important intermetallic formed during soldering reactions is Cu_3Sn, the formation of which is closely associated with Cu_6Sn_5. After Cu_6Sn_5 precipitation, a planar Cu_3Sn layer with a thickness more than 250 nm was observed after reflowing pure Sn on a Cu substrate for 4 minutes at 245 ^oC [85]. The Cu_3Sn thickness suggested the formation of Cu_3Sn was initiated at the earlier stage of the liquid/substrate reaction. This was further evidenced by a TEM study that showed Cu_3Sn formed after 4~5 seconds of reflow of eutectic SnBi solder at 170 ^oC, as shown in Fig. 12 [96]. Because the eutectic temperature of Sn-Bi alloys is much lower than that of pure Sn and the difference of driving force for formation of Cu_6Sn_5 and Cu_3Sn increases as the temperature decreases, it is reasonable to expect both Cu_3Sn and Cu_6Sn_5 can be formed after a very short reflow at the interface between most Sn-based Pb-free solder alloys and Cu.

The competitive growth of Cu_6Sn_5 and Cu_3Sn is both diffusion and reaction controlled and multiple parameters such as reaction temperature, reaction time and the surface of the substrate must be considered [96], which can be discussed using the schematic diagram of the possible inter-diffusion fluxes in a

Cu/Sn/Cu sample in Fig. 13 [93]. Firstly, it is clear that, after a short time of liquid state reaction, Cu_6Sn_5 forms in a scallop shape with nano-scale channels in between and the Cu_3Sn forms in a planar morphology with closer grain boundaries than that in the Cu_6Sn_5 layer [85, 96]. These channels are occupied by the Cu flux from the Cu substrate to Cu_6Sn_5 layer. As a result, it is difficult for Sn to pass through these channels and hence, Sn needs to diffuse through the IMCs to react with Cu at the substrate side. During the liquid reaction, the higher driving force for formation results in the Cu_6Sn_5 precipitating preferentially. This can be observed from the movement of the interface in a Cu/Sn/Cu sandwich sample during the transient liquid reaction [93]. Whilst Sn remains, the growth of Cu_3Sn is slow and the Cu_3Sn thickness does not increase clearly during the reaction time from 30 to 60 minutes.

After the liquid state reaction, Cu_6Sn_5 and Cu_3Sn keep growing during the solid state reaction. Previous research on the solid state reaction between Sn and Cu has been well documented in [77]. Here, it should be noted that during the solid state reaction between Sn and Cu, monoclinic Cu_6Sn_5 can be formed at temperatures as low as -2 ^oC. Moreover, at around room temperature, Tu [97, 98] and Tu and Thompson [99] reported Cu is the dominant diffusion species, likely through the grain boundary diffusion through η'-Cn_6Sn_5 and interstitial diffusion in Sn; while other studies at temperature around 200 ^oC reported the volume diffusion of Sn should be dominant. Currently, to the best of our knowledge, there is no indisputable conclusion on the diffusion between Cu and Sn reaction couples. This is likely because of the relatively high homologous temperature of Sn at solid state reaction temperatures, which in turn affects the dominant diffusion elements (Cu or Sn) and the diffusion mechanisms.

In a real solder joint, typically a layer of pre-formed Cu_6Sn_5 and Cu_3Sn grows during the solid state reaction at a temperature below or around 150 ^oC. In this case, the solid state growth of Cu_6Sn_5 is dependent on the morphology of the previously formed Cu_6Sn_5, as well as the competitive growth with Cu_3Sn at the reaction temperature. If the prior Cu_6Sn_5 is of a nodular morphology, planarization of the Cu_6Sn_5 layer occurs first [100]. During the solid state aging at 175 ^oC, a bulk diffusion mechanism was suggested to be dominant in the growth of Cu_6Sn_5 [100]. On the other hand, at 140 ^oC a mixed grain boundary and volume diffusion

mechanism was suggested to dominate the growth of Cu_6Sn_5 [100]. However, no matter what morphology the prior Cu_6Sn_5 has, growth of Cu_3Sn is always controlled by grain boundary diffusion. Different to the observation during the liquid state reaction, during the solid state reaction, the thickness of Cu_3Sn grows quickly to be comparable to that of Cu_6Sn_5, at the expense of Cu_6Sn_5 [100, 101]. This is because Cu_3Sn is possible to form in two ways: through the reaction of $3Cu+Sn=Cu_3Sn$ at the interface between Cu and Cu_3Sn, and through the reaction of $9Cu+Cu_6Sn_5=5Cu_3Sn$ at the interface between Cu_6Sn_5 and Cu_3Sn. At the interface between Cu and Cu_3Sn, the release of Cu atoms from Cu unit lattices is difficult at low homogenous temperature of Cu and the fast grain boundary diffusion of Sn through the Cu_3Sn layer promotes the reaction of $3Cu+Sn=Cu_3Sn$ [96]. Moreover, at an aging temperature typically close to 150 ^oC, the decomposition of Cu_6Sn_5 at the interface between Cu_6Sn_5 and Cu_3Sn can be readily activated [97]. In some studies, the abnormal growth of Cu_6Sn_5 has been reported during solid-state aging as shown in Fig. 14 [101], which is undesirable because of possible stress concentrations. A recent study suggested the preferential growth of Cu_6Sn_5 along the grain boundary of the solder matrix is responsible for this abnormal growth [101]. Based on the EBSD analysis and a plot of the IMC thickness, it has been proposed that Sn diffuses faster along the [0001] direction of Cu_6Sn_5 crystals [101], which is reasonable for a hexagonal-like Cu_6Sn_5 crystal but no direct evidence has been given.

4.1.2 Formation between common solder alloys and polycrystalline Cu

In binary Sn-Pb solders, the morphology and formation of Cu_6Sn_5, and/or Cu_3Sn, are affected by the ratio between the Sn and Pb [83, 102]. The lower the Pb content and the lower the reaction temperatures, the easier it is for Cu_6Sn_5 to form and vice versa. During the interfacial reaction of eutectic Sn37Pb solder and Cu substrates, a round scallop-like Cu_6Sn_5 forms after soldering [83]. According to the force balance at the triple point of Cu_6Sn_5, solder and the Cu substrate interface, the roughness of Cu_6Sn_5 scallops is dependent on the interface tension between the molten alloys and solid Cu substrates: the smaller the surface tension of the molten solder, the smaller interface tension and the higher likelihood of a round scallop-like morphology forming; on the other hand, a higher surface tension will result in higher interface tension and the formation of faceted Cu_6Sn_5 scallops [83, 102]. The Cu_3Sn phase only appeared as the reaction temperature was increased to 290 ^oC, which can be explained as the driving force for Cu_6Sn_5 formation being higher than that

of Cu_3Sn at low temperatures and the increase on reaction temperature reduces the difference between the driving forces. Moreover, higher Pb content (73wt%) reduces the supply of Sn and favours the formation of Cu_3Sn [83]. From the size distribution of Cu_6Sn_5 formed between Sn45-Pb alloys and a Cu substrate, the growth of Cu_6Sn_5 was found to obey the non-conservative FDR model within a reflow period up to 8 minutes [102]. Prakash and Sriharan reported a time-dependent growth behaviour of Cu_6Sn_5, but the purely volume diffusion controlled growth mechanism was not reached after a reaction of 330 minutes. Moreover, a (101) or (102) growth texture of Cu_6Sn_5 at the interface between Sn27-Pb and Cu interface was reported. Using EBSD techniques, Yang et al. reported the Cu_6Sn_5 formed at the eutectic Sn37-Pb solder and Cu substrate interface is of a (001) Cu_6Sn_5 growth texture after reflow at 200 ^oC; as the temperature increased from 200 ^oC to 280 ^oC, a (101) growth texture formed [103]. By varying the reaction temperature and subsequent aging treatment, the (101) texture formed at 280 ^oC was found to remain after a second reflow at 200 ^oC for 600 minutes [103].

Most lead-free solders are Sn-rich alloys with the Sn content greater than 90wt% and melting temperatures close to the eutectic Sn37-Pb solder. Because of the Sn-rich nature of near-eutectic Pb-free solders, the interfacial formation of Cu_6Sn_5 is similar to the reaction between pure Sn and Cu. During the reaction between Sn-Cu alloys and Cu substrates, Cu_6Sn_5 is also the first phase to form during the interface reaction, which was proven by observing the interface reaction between near-eutectic Sn-Cu solders and Cu substrates [104, 105]. A round scallop-like Cu_6Sn_5 was reported to form, and then coarsen and facet as the reflow time increased. A linear relationship between the square root of reflow [104] and aging [105, 106] time and intermetallic thickness was found, which suggests a volume diffusion controlled growth mechanism. Cu_3Sn was only found by SEM techniques after an extended reflow time (5 minutes) [104], or after a certain period of aging [105, 106]. After aging for 1000 hours, cracks along the interface between the Cu_3Sn layer and Cu substrate were observed [106]. Considering the location of crack formation, this cracking was highly likely to be related to the formation of Kirkendall voids during the growth of the Cu_3Sn phase. As the Cu content was increased to 3 and 4wt%, the Cu_6Sn_5 that forms at the solder/substrate interface remains scallop-like, but with a more faceted morphology [107]. As the Cu content was increased further from the eutectic point to

7wt%, the Cu_6Sn_5 has a faceted rod-like morphology [107]. Moreover, for an as-dipped Sn-3Cu and Cu reaction couple, Cu_3Sn cannot be detected by SEM techniques; while Cu_3Sn can be clearly observed in the as-dipped Sn-4/7Cu and Cu reaction couples [107].

During the interface reaction between near-eutectic Sn-Ag(-Cu) solders and Cu substrates, a rounded scallop-like morphology was commonly reported for the interfacial Cu_6Sn_5 [108]. Recently, Cho et al. reported that the addition of 3wt% Ag could reduce the ripening process and hence the Cu_6Sn_5 grain size compared to Ag-free Sn-0.5Cu and Sn-1Ag-0.5Cu [109]. It was also observed that the addition of Ag changed the scallop-like Cu_6Sn_5 into a more flat morphology, which is an indicator of a reduction in the interfacial energy responsible for the reduced ripening process [109]. The growth exponent of Cu_6Sn_5 in an interface reaction less than 30 minutes is close to 1/3 [84, 110, 111], indicating a grain boundary diffusion control mechanism. Increasing the reaction time resulted in further growth of Cu_6Sn_5, but the volume diffusion controlled growth mechanism was not observed [84]. During the solid state reaction, a layered IMC structure was commonly observed [100, 101]. Using the EBSD technique, the Cu_6Sn_5 formed between the Sn-3.8Ag-0.7Cu and Cu interface at a reflow temperature close to 250^oC was found to be of a (001) growth texture [111]; while a 30 ^oC increase in temperature from 250 ^oC to 280 ^oC resulted in the change of growth texture from (001) to (101) at the interface between pure Sn and Cu or Sn-3.5Ag alloy and Cu [84, 112], as shown in Fig. 15 [84]. It is worth noting that, in a Sn-3.8Ag-0.7Cu and Cu reaction couple, a thin film of Cu_3Sn was reported to form prior to the precipitation of Cu_6Sn_5 during the reflowing reaction [113]. This has been explained as a result of the action of the flux, which has dissolved the Cu from the substrate and Sn from the solder to make a localised concentration with high Cu content.

4.1.3 Effects of selected alloying elements

The effects of alloying elements on the interface formation of Cu_6Sn_5 have been widely studied and comprehensively reviewed [4, 77, 78]. Normally, the elements that have remarkable solubility in the IMC layer affect the interfacial Cu_6Sn_5 formation more significantly [114]. A comprehensive review of the effect of alloying elements on the interfacial formation of Cu_6Sn_5 is beyond the scope of this paper and only the

effect of Ni and Zn on the interfacial formation of Cu_6Sn_5 has been summarised because these elements have a significant effect on the phase stability, solidification and mechanical properties of Cu_6Sn_5.

A trace Ni addition to the Sn-0.7Cu alloy has demonstrated significant improvements on the soldering properties such as better flow characteristics and a microstructure closer to a complete eutectic [48-50]. As a result, the interface reaction in Sn-Cu-Ni system received great attention [115-117]. It has been found that a trace amount of Ni results in the formation of Cu_6Sn_5 with a flat morphology [104, 105], refined grain size [20], and the addition of 0.05wt% Ni in Sn-0.7Cu resulted in the minimum Cu_6Sn_5 thickness after soldering and subsequent aging [105]. Moreover, Ni was reported to reduce the formation of Cu_3Sn and hence the associated formation of Kirkendall voids [104]. In the Sn-Ag-Cu system, the effect of Ni on the inhibition of Cu_3Sn growth in Sn-2.5Ag-0.8Cu was reported by Wang et al., and a Ni concentration as small as 0.01wt.% was found to effectively retard Cu_3Sn growth even after 2000 hours of aging [118]. By synchrotron X-ray fluorescence, the Ni concentration in the Cu_6Sn_5 layer on the substrate side was found to remain constant even after being annealed for 500 hours [119], which impedes the growth of Cu even after significant annealing. Laurila et al. attributed this effect of Ni to increasing the diffusion of Sn (the dominant diffusion species in Cu_6Sn_5) and decreasing the diffusion of Cu (the dominant diffusion species in Cu_3Sn), as a result the formation and growth of Cu_3Sn is impeded [77]. In addition, the effect of Ni addition on growth orientation of Cu_6Sn_5 between Sn-0.7Cu/Cu [120] and Sn-3/4/7Cu [107] and poly-crystalline Cu was investigated. After the addition of 0.05wt% Ni, a strong (101) pole figure was observed for the Cu_6Sn_5 formed on poly-crystalline Cu [107, 120]. Moreover by X-ray diffraction, it was found Ni increases the (101) growth but decreases the (102) growth of Cu_6Sn_5 crystals [120].

Zn additions have also been shown to have a strong effect on the interface reaction between Sn-0.7Cu and Cu substrates. It was found that the addition of 0.2wt% Zn in Sn-0.7Cu solder effectively reduced the IMC thickness, as well the formation of Cu_3Sn [53]. After the addition of 1wt% Zn, CuZn IMCs, instead of Cu_6Sn_5, formed at the solder/substrate interface and aging did not increase the thickness of the CuZn layer [53]. Moreover, the interface reaction between Sn-based solders and Cu substrates is extremely sensitive to

the Zn content in the solder [121]. If the concentration of Zn in the solder is higher than 2wt%, a reaction occurs between the Cu and Zn rather than Sn, producing Cu-Zn binary IMCs.

4.1.4 On poly-crystalline Ni

Ni is commonly used as reaction barrier on Cu substrates or metallization material on Si. During the interface reaction between pure Sn and Ni, a layer of Ni_3Sn_4 intermetallic forms [122, 123]. However, the Cu content in solders has a remarkable effect on the final product of the interface reaction on a Ni substrate. When Cu content was higher than 0.4wt%, only Cu_6Sn_5 would form; when Cu content was between 0.2 and 0.4wt%, both Cu_6Sn_5 and Ni_3Sn_4 formed; if the Cu content was lower than 0.2wt%, Ni_3Sn_4 formed [124]. Given that the Cu content in most existing Sn-Cu and Sn-Ag-Cu solders is higher than 0.4wt%, Cu_6Sn_5 is also the dominant interfacial IMCs to form on a Ni substrate. In this case, a relatively thin and continuous Cu_6Sn_5 with a rod-like morphology forms on Ni substrates at the initial stage [116, 125]. Different to that on Cu substrates, the Cu_6Sn_5 formed on Ni substrates demonstrates a detachment behaviour during the extended liquid/solid reaction [126]. As reaction time increased, the Cu_6Sn_5 layer with coarse grains detached into the solder matrix and a Cu_6Sn_5 layer with finer grains starts to grow at the solder/substrate interface. A further increase in reaction time leads to the formation of Ni_3Sn_4 and the newly exposed Cu_6Sn_5 disintegrates [126]. The detachment time is dependent on the amount of solder alloy [126], which has been confirmed in another study on the interface reaction between Sn-Cu solders with Cu content from 0.3wt% to 3wt% [127]. The composition-dependent detachment behaviour is due to the growth of Cu_6Sn and is controlled by the amount of Cu available for interface reaction and when the Cu supply depletes, the formation of new Ni-Sn phases induce the detachment of the IMCs layer.

4.2 In 3 dimensional arrangement

In the electric packaging industry, the size of a BGA solder ball is in the range of 500 μm to 100 μm. Below 100 μm, solder paste or electroplated solder are used to manufacture the so-called micro-bumps in 3D ICs. The reduced size of solder joints raises metallographic issues and as a result there is no commercial product that utilises 3D packaging technology available in the market yet. Pioneering research is continuously reporting that Cu_6Sn_5 will be present at a higher volume fraction than in BGA solder joints. Indeed,

understanding the properties of Cu_6Sn_5 formed in such small scale micro-bumps is the key to address the reliability issues induced by reduced size of solder joints.

4.2.1 On single-crystalline substrates

A micro-bump in newly developed 3D ICs is expected to be sub-micron in scale, which is comparable to or even smaller than the grain size in Cu substrates. In this case, the grain boundaries in the substrate will be absent and the knowledge on the growth of Cu_6Sn_5 on a single-crystalline Cu substrate is of great importance for the understanding of the metallurgical features in 3D ICs packaging. Suh et al. firstly observed that the morphology of the Cu_6Sn_5 at the interface between a Sn45-Pb alloy and (001) single-crystalline Cu substrate was found to be of a rooftop-like morphology as shown in Fig. 16 [128, 129]. Using the synchrotron white beam micro-X-ray histogram, two crystal relationships were observed: firstly, the $[\bar{1}01]$ direction of most Cu_6Sn_5 grains is perpendicular to the [001] direction of Cu, or say, lying in the (001) plane of Cu; secondly, the $[\bar{1}01]$ direction of most Cu_6Sn_5 grain is parallel to the [110] or $[\bar{1}10]$ direction in the (001) plane of Cu [128]. The same orientation relationship was observed in the Cu_6Sn_5 formed between pure Sn and a single-crystalline Cu substrate [130]. The observed orientation relationship was found to depend on the reaction time: at the very early stage of the reaction, the random nucleation does not result in any orientation relationship; as the reaction time increases, Cu_6Sn_5 texture becomes observable; and a further increase in reaction time leads to damage in Cu_6Sn_5 texture due to the formation of Cu_3Sn [130].

Subsequently, the morphology and crystal orientation of Cu_6Sn_5 has been investigated between pure Sn and (001), (011), (111) and (123) single-crystalline Cu substrates [129]. In addition to the above observation on (001) single-crystalline Cu, a mis-orientation angle of 60^o between the rooftop-like Cu_6Sn_5 grains on the (111) Cu was found with indexed orientation relationships as $(102)_{Cu6Sn5}//(111)_{Cu}$ and $(010)_{Cu6Sn5}//(111)_{Cu}$. As reaction time and aging time increased, the rooftop-like morphology changed to a scallop-like one, due to the formation of Cu_3Sn during the liquid-solid reaction and the difference in diffusion speed of Cu atoms through the rooftop-like Cu_6Sn_5 layer during solid aging at 180 ^oC (the thicker the Cu_6Sn_5 the slower diffusion of Cu), respectively [129]. The observed orientation relationships and elongation direction of Cu_6Sn_5 were explained by analysing the misfit between Cu atoms in Cu_6Sn_5 and different crystal planes of

Cu substrates: minimisation of misfit between Cu atoms reduced the interfacial energy between the Cu_6Sn_5 and Cu substrate [128-130].

Because of the strong effect of crystal orientation of the Cu substrate, the Cu_6Sn_5 formed on different Cu crystal planes will be of variable orientations and morphologies. To ensure the service reliability of micro-bumps, a uniform microstructure is desirable, which has been achieved by the design of single-crystalline substrates. Hsiao et al. grew the Cu_6Sn_5 on [111]-oriented nano-tube Cu substrates with a size up to 20 microns [1]. In this case, the Cu_6Sn_5 formed during reflow was of a scallop-like morphology with a (001) growth orientation. Moreover, the formation of Kirkendall voids was largely impeded because high density grain boundaries in the nano-tube Cu substrate played a role as vacancy sinks.

The morphology change and the crystal orientation of Cu_6Sn_5 on single-crystalline Ni substrates has also been reported [8]. The [001] directions of $(Cu,Ni)_6Sn_5$ elongated perpendicularly to each other on the (001) plane of Ni; and the $(1\bar{2}0)_{(Cu.Ni)6Sn5}//(1\bar{1}1)_{Ni}$ and $[001]_{(Cu,Ni)6Sn5}//[110]_{Ni}$ orientation relationship was identified [8]. This orientation relationship contributed to the close matching of the Cu sub-lattice from the $(1\bar{2}0)$ plane of $(Cu,Ni)_6Sn_5$ with Ni atoms from $(1\bar{1}1)$ of Ni. In addition to the growth orientation of Cu_6Sn_5 on single-crystalline Cu and Ni substrates, the growth orientation of Ag_3Sn on single-crystalline Ag substrates has recently been reported and it was found that regular Ag_3Sn grains with parallel edges grew on (001) single-crystalline Ag substrates and faceted scallop-type Ag_3Sn grains irregularly formed on poly-crystalline Ag and (011) and (358) single-crystalline Ag [131], which was due to the matching of Ag atoms between the Ag_3Sn and Ag substrate.

4.2.3 Electro- and thermo- migration effects

Electro-migration (EM) has been considered to be a reliability problem since flip chip technology was developed. The recent development of the 3D packaging technique further raises thermo-migration (TM) as a reliability challenge because the increased current density and associated Joule heating in micro-bumps result in a typical thermal gradient of 1000 ^{o}C/cm [3]. In this case, the driving forces for EM and TM are quite comparable and hence both EM and TM in a solder joint must be considered to ensure the reliability of

micro-bumps in 3D ICs [132]. Previous studies on the effect of EM on solid state IMCs formation have shown that Cu_6Sn_5 and Cu_3Sn in eutectic SnAgCu are transferred from the cathode to the anode side, which leads to void formation and impeded IMCs growth at the cathode side as shown in Fig. 17 [133]. This EM driven migration of atoms from the cathode side to the anode side, is known as the polarity effect. In addition to the polarity effect, the electric current through a micro-bump also results in Joule heating, especially when current crown occurs. The heating then causes TM in charged and neighbouring uncharged micro-bumps. Under a thermal gradient, the formation of Cu_6Sn_5 is essentially affected by the diffusion of both Sn and Cu atoms. Cu_6Sn_5 was found to grow preferentially at the cold side of micro-bumps during the reaction between Sn-2.5Ag and Cu of a hot plate experiment [134], as shown in Fig. 18. In the solid state, the asymmetric growth of the IMC layer occurs in a similar fashion.

5. Thermo-mechanical properties

Because of the increasing volume fraction of IMC in solder joints, the thermal expansion and mechanical properties of Cu_6Sn_5 play an increasingly important role on the integrity of the aforementioned solder joints. In this section, the thermal expansion and mechanical properties (elastic modulus, hardness, creep and fracture behaviour) of Cu_6Sn_5 are summarised with particular attention to the relationship between crystal structure, temperature and alloying elements.

5.1 Thermal expansion of Cu_6Sn_5

The difference in the coefficients of thermal expansion (CTEs) between constituent materials leads to the generation of thermal stress during the manufacture and service of a solder joint. However, research on the thermal expansion behaviour of Cu_6Sn_5 is relatively limited. Early research gave discrete measurements on the thermal expansion of Cu_6Sn_5 at temperatures between 60 and 160ºC using step heating dilatometry [135] and 100 to 250ºC by *in-situ* synchrotron diffraction [136]. First principle computation suggested a non-linear thermal expansion behaviour of Cu_6Sn_5 [137], which was confirmed experimentally [135, 136]. Using step-heating synchrotron X-ray diffraction, a volume shrinkage has been recently observed during the hexagonal to monoclinic polymorphic transformation at temperatures around 186ºC, as shown in Fig. 19 [138]. This observation is in contrast to the order of density of Cu_6Sn_5 at room temperature (8.270 g/cm^3 for the monoclinic phase and 8.448 g/cm^3 for hexagonal phase) [15], and suggests a strong dependence of the

thermal expansion of hexagonal Cu_6Sn_5 on temperature. Moreover, trace additions of Ni have been found to reduce the overall thermal expansion of Cu_6Sn_5 [138, 139], with a preferential reduction along the a-axis as the Ni content increases from 4.6 at% to 17.2 at% [139].

The effect of Zn, Au and In on the thermal expansion of high-purity stoichiometric Cu_6Sn_5 has also been studied by synchrotron diffraction and dilatometry techniques [36]. It was found that Zn reduces the overall thermal expansion of Cu_6Sn_5 with a preferential reduction of thermal expansion along the a-axis; Au reduced the overall thermal expansion along both a and c axes; and In has a weak effect on the overall expansion of Cu_6Sn_5 [36]. Because the reported CTE of Cu_6Sn_5 (from 18.3 [135] to 32.0 [138] ppm/^oC) is larger than that of commonly used substrate materials (16.7 ppm/^oC for Cu and 2.1 ppm/^oC for Si), it is desirable to reduce the thermal expansion of Cu_6Sn_5 and hence to minimize the internal thermal stress of a solder joint.

5.2 Mechanical properties of Cu_6Sn_5

5.2.1 Elastic modulus and hardness of Cu_6Sn_5

The elastic modulus and hardness are the most investigated mechanical properties of Cu_6Sn_5. Because of the lack of a standard test procedure, early research showed large variations and the mechanical properties of bulk Cu_6Sn_5 compared to Cu_6Sn_5 formed at the interface region of a solder joint [140]. Nanoindentation has been widely used to characterize the mechanical properties of Cu_6Sn_5 in a solder joint, due to its' capability to probe the mechanical properties of a small volume of material. Originally, nanoindentation was used to extract the mechanical responses of constituent phases in solder joints [141, 142]. However, because the indentation location is difficult to identify using conventional characterization techniques such as SEM, these nanoidnetation results also had considerable variation. Atomic force microscopy (AFM) was then used in conjunction with nanoindentation to reduce the uncertainties in measurement. Using Sn–Cu and Sn–Ni diffusion couples, Yang et al. measured the elastic modulus and hardness of Cu_6Sn_5 in the directions lateral or perpendicular to the diffusion direction, and reported isotropic elastic modulus and hardness [143]. By reflowing and aging Sn–3.5Ag solder on a Cu plate, Deng et al. prepared IMC layers with a thickness greater than 50 μm and measured the elastic modulus and hardness of several IMCs including Cu_6Sn_5 and Cu_3Sn [10, 144]. Considering the effects of the soldering process, Tsukamoto et al. investigated the effects

of multiple reflows on the mechanical properties of Cu_6Sn_5 and $(Cu,Ni)_6Sn_5$ formed in Sn-0.7Cu(-0.05Ni)/Cu BGA solder balls [145]. It was found that the number of reflows had little influence on the elastic modulus and hardness of Cu_6Sn_5, but the substitutional Ni increases the elastic modulus and hardness of Cu_6Sn_5 [145], which is in agreement with previous results obtained on a Ni substrate [146]. Nanoindentation has also been used together with conventional tensile testing to investigate the mechanical properties of Cu_6Sn_5, as well as the fractured phase in Sn-0.7Cu/Cu solder joints at variable strain rates [147]. Aging only slightly increased the elastic modulus and hardness of Cu_6Sn_5 [147]. Moreover, nanoindentation also revealed an increase in the modulus and hardness of these cracked phases induced by high strain rates [147].

The relationship between the mechanical properties and crystal orientation of Cu_6Sn_5 has been recently investigated using nanoindentation together with the EBSD technique. Song et al. firstly conducted nanoindentation on Cu_6Sn_5 in reflowed solder joints, and Cu_6Sn_5 grown directionally by a liquid-electromigration technique [148]. It was found that the close packed (110) crystal plane of the directionally grown Cu_6Sn_5 has the highest elastic modulus and hardness values. Moreover, the addition of a small amount of Ni or Ag in the solder alloys did not affect the anisotropic mechanical properties of Cu_6Sn_5 [148]. On the other hand, nanoindentation on the basal (001) crystal plane of Cu_6Sn_5 directionally solidified from a Sn-4Cu alloy yielded the highest indentation modulus and hardness [149, 150], which is in agreement with the result obtained on Cu_6Sn_5 micro-pillars prepared by the ion-lathe technique[151].

In a recent study, the indentation on the direction perpendicular to the Sn-3.5Ag/Cu interface (E≈155 GPa and H≈ 8.2 GPa for Cu_6Sn_5-[N]) reveals higher elastic modulus and hardness than that obtained in the direction parallel to the Sn-3.5Ag/Cu interface (E≈ 133 GPa and H≈ 6.7GPa for Cu_6Sn_5-[P]) [152]. As discussed in Section 4, there is a (001) growth texture of Cu_6Sn_5 at the Sn-3.5Ag/Cu interface [112], which means interfacial Cu_6Sn_5 has the highest elastic modulus and hardness on the crystal planes close to the basal (001) plane. A plot of the elastic modulus and hardness against the mis-orientation angles between the normal of a crystal plane and the c-axis of hexagonal Cu_6Sn_5 is shown in Fig. 20, in which the (001) plane of

Cu_6Sn_5 is more resistant to both plastic and elastic deformations than other crystal planes [149]. The faceted hexagonal structure of Cu_6Sn_5 (a= 4.190 Å, c= 5.087 Å) should be responsible for the anisotropic mechanical properties as the indentation on a basal plane is likely to induce the movement of more atoms from their original position [149].

The temperature dependence of Cu_6Sn_5 mechanical properties were investigated by nanoindentation at elevated temperatures. Using stoichiometric samples, the reduced modulus and hardness of $Cu_{6-x}Ni_xSn_5$(x = 0, 0.5, 1, 1.5, 2) were found to decreases linearly and exponentially, respectively, as temperature increases [149]. Contrasting results have been reported on the Cu_6Sn_5 formed at the interface between Sn-3.5Ag solders and Cu substrates, that the Young's modulus and hardness of Cu_6Sn_5 has a weak dependence on the temperature [152]. As temperature increased from 150 ^oC to 175 ^oC, the Young's modulus increased from 144±17 GPa to 160±30 GPa, which was attributed to the η to η′ phase transformation at 150^oC [152]. According to previous studies [26, 27] and the experimental conditions in [152], the majority of Cu_6Sn_5 should be transformed into the monoclinic structure prior to the indentation test. In another study, the elastic modulus of Cu_6Sn_5 formed in Sn-3.9Ag-0.7Cu/Cu solder joints was also found to be weakly dependent on temperature, but the hardness of Cu_6Sn_5 significantly decreased at elevated temperatures [153]. Therefore, considerable discrepancies on the mechanical behaviour of Cu_6Sn_5 at elevated temperatures exists.

Alloying elements in solders also demonstrated significant effects on the mechanical properties of Cu_6Sn_5, which is generally dependent on chemical composition. A good example is the effect of Ni additions on the mechanical properties of Cu_6Sn_5. It was reported that, after aging, the hardness and elastic modulus of the Ni-free Cu_6Sn_5 in the Sn-Ag-Cu and OPS Cu solder joint are constant at approximately 5.7 GPa and 97.0 GPa, respectively [146]. However, for $(Cu,Ni)_6Sn_5$ at the interface between Sn-Ag-Cu solders and ENIG substrates, the elastic modulus changed from 207 GPa to 146 GPa and the hardness decreased from 10.0 GPa to 7.3 GPa [146]. According to previous studies [154], the addition of Ni has shown a diverse range of effects on the mechanical properties of Cu_6Sn_5 and the measured mechanical properties of $(Cu,Ni)_6Sn_5$ have varied largely, which is highly likely due to Ni composition gradients in the Cu_6Sn_5 at the solder/substrate

interfaces. The Ni content of $(Cu,Ni)_6Sn_5$ in [145] was measured and found to be close to 5wt% and relatively homogeneously distributed [155]. However, the Ni content in $(Cu,Ni)_6Sn_5$ in [146] was likely to be inhomogenously distributed, due to the solid state diffusion of Ni from the substrate during ageing [154]. This is supported by the large discrepancy of reported Ni concentrations in Cu_6Sn_5. For instance, Cu_6Sn_5 at the interface between pure Sn and Ni has a Ni concentration of 16.7at% [156]; at the interface between Sn-0.7Cu solder and Ni substrates, the Ni concentration changed from 15.3at% to 22.2at% after ten minutes of reflow at 255 ^oC [157]; in Sn-0.6Cu-0.05Ni/Cu reaction couples, the Ni content was constant at 4.3at% [104], which was close to 5wt% as measured in [145]. Moreover, a Ni content gradient has been directly detected in Sn-Ag(-Ni)/Cu solder joints [158] and diffusion samples [159]. On the other hand, synchrotron X-ray micro-XRF confirms a relatively homogeneous Ni distribution in Sn-0.7Cu-0.05Ni/Cu solder joints after 500 hours aging [119]. Compared to the calculated maximum solubility of Ni in Cu_6Sn_5, 27at% [6], the measured Ni distribution in Cu_6Sn_5 has been shown to have great variation over a range of studies. In order to investigate the mechanical properties of Cu_6Sn_5 with variable Ni concentrations, direct cast samples with known Ni content have been prepared and it was found that the elastic modulus and hardness increased linearly with the Ni content in Cu_6Sn_5 [160]. In addition, Zn, In and Au were also found to increase the elastic modulus and hardness of Cu_6Sn_5, as shown in Fig. 21 [161]. It can be seen that, as the Zn and In content increases, the elastic modulus and hardness of Cu_6Sn_5 increases; while the addition of Au only slightly increases the hardness of Cu_6Sn_5.

In addition to the reported experimental investigations on the mechanical properties of Cu_6Sn_5, the elastic modulus of Cu_6Sn_5 has also been determined by theoretical computation. Lee et al. reported that the computed elastic modulus of Cu_6Sn_5 is 120 GPa [162]. In general, the nanoindentation results agree well with the computational results. Moreover, recent first principle calculation results indicated that the hexagonal-like monoclinic Cu_6Sn_5 was stiffer along the c-axis [137, 163], which is in agreement with the experimental result from the nanoindentation on a Cu_6Sn_5 micro-pillar[151], interfacial Cu_6Sn_5 [152] and directionally solidified Cu_6Sn_5 [149, 150]. To date, computational calculations on the effect of alloying elements on Cu_6Sn_5 mechanical properties are not yet available in the literature. This may be due to the

difficulties in the determination of the stable crystal structure of these ternary IMCs as well as the complications involved in the computation. However, all alloying elements have been experimentally reported to increase the elastic modulus and hardness of Cu_6Sn_5, by inducing volume shrinkage [36, 38, 138, 139] and substitutional defects in the unit cell of Cu_6Sn_5.

Another intermetallic commonly formed during the interface reaction of Sn-Cu solders and Cu substrates is Cu_3Sn, whose elastic modulus and hardness were also determined by nanoindentation [10, 143]. In addition, An et al. reported that the elastic modulus of Cu_3Sn was 147GPa by a first principle computation [164]. This computational result is in reasonable agreement with the experimental results as summarized in Table 2.

5.2.2 Creep and fracture behaviour of Cu_6Sn_5

The creep of Cu_6Sn_5 and other common IMCs formed during lead-free soldering was recently investigated using nanoindentation [165, 166]. It was found that Cu_6Sn_5 has the highest creep exponent compared to other intermetallic compounds [165]. Using the Cu_6Sn_5 in directionally solidified Sn-4Cu(-0.05Ni) alloys, Cu_6Sn_5 was found to have the lowest creep resistances on the crystal planes close to the (110) and (100) planes, and the largest creep resistance on the (001) plane [149]. The addition of Ni increased the creep stress exponents on all crystal planes and significantly reduced the difference between the creep exponents on different crystal planes [149]. Similar creep behaviour at room temperature has been observed in recent studies on Cu_6Sn_5 in cast and reflowed samples [149, 167]. In addition, the creep stress exponents of Cu_6Sn_5 and $Cu_{5.5}Ni_{0.5}Sn_5$ were found to decrease as the temperature increased from 25 to 150^oC and Ni was found to reduce the creep of Cu_6Sn_5 at 25^oC, but increase the creep of Cu_6Sn_5 at 125 and 150^oC. However, based on the creep displacement during the dwell time at peak load of nanoindenation, the creep of interfacial Cu_6Sn_5 between Sn-Ag-Cu and Cu substrates was reported to have a weak dependence on the temperature [167]; while another work on Sn-Ag-Cu/Cu reported decreased hardness of Cu_6Sn_5 [153].

The fracture behaviour of monoclinic and hexagonal Cu_6Sn_5 were firstly observed using microhardness indentation on stoichiometric bulk samples [168]. The crystal structure does not affect the crack pattern under a Vicker's indenter and all cracks were initiated near the corners of the indenter, where larger

indentation strain and stress were induced. Using nanoindentation with a flat tip, Jiang et al. studied the fracture behaviour of Cu_6Sn_5 micro-pillars fabricated using a focused iron beam (FIB) [169]. From the load-displacement curves, crack-induced pop-ins were found to occur at multiple applied loads, which indicates a possible dependence of fracture initiation on the crystallographic orientation of Cu_6Sn_5[169]. The fracture morphology of Cu_6Sn_5 is commonly of a typical brittle fracture.

Using an *in-situ* micro-hardness tester installed with an SEM function, the Cu_6Sn_5 formed at the Sn-4Ag solder and Cu substrate interface was found to fracture in two possible patterns: either underneath the indenter associated with the appearance of secondary cracks, or at a location in between the substrate and indenter due to the plastic deformation on an adjacent Cu_6Sn_5 grain [170]. The difference between these two fracture patterns is more likely to be related to the morphology of Cu_6Sn_5, as the long rod-like Cu_6Sn_5 cracks at the end of grains and the short rod-like Cu_6Sn_5 cracks at the centre of grain [170]. However, in both cases, fractures were initiated in a direction parallel to the solder/substrate interface where a (001) Cu_6Sn_5 growth texture formed [107], suggestive of a (001) slip plane of Cu_6Sn_5 [170]. In our previous study [149], a conical tip was used to induce a uniform stress distribution and initiate the crack on the crystal plane parallel to the c-axis of Cu_6Sn_5. As shown in Fig.22, for the Ni-free Cu_6Sn_5, the primary cracks initiated in a direction perpendicular to the c-axis, which is approximately in the (001) plane of Cu_6Sn_5, and secondary cracks were observed parallel to the c-axis of Cu_6Sn_5 [149]. After Ni addition, the resistance of the intermetallic to cracking appeared to be increased substantially.

6. The role of Cu_6Sn_5 in solder joint integrity

While the interfacial formation and thermo-mechanical properties of Cu_6Sn_5 have been intensively characterized, the role of Cu_6Sn_5 in the deformation of solder joints subject to the mechanical and/or thermal stresses has received relatively less attention. A conventional BGA or THP solder joint consists of a ductile solder matrix and brittle IMC layer at the interface between solder and substrate. Chwala has proposed a hypothesis that as the strain rate increases, a transition from ductile fracture controlled by the solder matrix to the brittle fracture controlled by the IMCs layer occurs [7]. At relatively low strain rates, the deformation of a Sn-Cu/Cu solder joint is controlled by the properties of solder alloys and ductile fractures typically

propagate in the solder matrix, associated with deformation of the solder matrix and a dimple morphology [171, 172]. As the strain rate increases, the ductile-brittle transition of the fracture of solder joints occurs and the fracture and the shear strength of Sn-Cu/Cu solder joints is controlled by the brittle IMC layer as shown in Fig. 23 [173]. In Sn-Ag-Cu/Cu and Sn-Ag-Cu/Ni reaction couples, the strain rate transition from solder-controlled ductile fracture to the IMCs-controlled brittle fracture has also been observed as strain rates increased [65, 174]. Moreover, at very high strain rates, the propagation of fracture moves to the substrate side, along the Cu_3Sn layer [175]. At high strain rates, it has been reported that short aging of around one hour can dramatically reduce the shear strength of Sn-Pb [176], Sn-Cu and Sn-Ag(-Cu) [177] solder joints. A recent study on the interfacial fracture in Sn-0.7Cu/Cu and Sn-4.0Ag-0.5Cu/Cu reaction couples have further demonstrated the increase in IMCs thickness leads the fracture of a Cu-solder-Cu sandwich solder joint from solder controlled fracture to IMCs controlled fracture[178]. It has been reported that the stabilized hexagonal phase and a non-(001) growth texture of interfacial Cu_6Sn_5 significantly improves the impact shear test of as-reflowed and aged Sn-Cu(-Ni)/Cu and Sn-Ag-Cu(-Ni)/Cu(-Zn) solder joints [179]. This is firstly because the stabilized IMC phase can avoid the undesirable volume expansion/shrinkage and accumulation of internal stress. Moreover the modification of the (001) growth texture can inhibit the crack propagation along the (001) slip plane of hexagonal Cu_6Sn_5 [107, 149]. In Fig. 24, it can be observed that as the strain rate and aging time increase, the fracture of solder is more likely to be brittle and propagate along the IMC layer [180].

Under thermal cycling conditions, there is a mismatch between the CTEs of substrates, IMCs and solder alloys leading to the generation of internal stress. In a BGA solder joint, cracks commonly initiate at the corner of a solder joint and propagate transgranularly or intergranularly along Sn grains. In a study on Sn-3Ag-0.5Cu alloys it was found that cracks initiate in the solder matrix and then possibly propagate to the IMC layer as the number of thermal cycles increases. As long as the crack reaches the IMCs layer, it propagates significantly faster than in the ductile solder matrix and results in the failure of whole solder joint [181]. Therefore, it is desirable to resist the crack propagation in solder matrix or improve the resistance of IMCs to the thermal stress. As mentioned above, the addition of certain amounts of alloying elements such

as Ni or Zn could effectively stabilize the crystal structure of Cu_6Sn_5 and prevent the formation of Cu_3Sn. However, further research is needed to investigate the effects of these alloying elements on the performance of solder joints subject to thermal stress.

Due to the high volume fraction of IMCs in micro-bumps, it is reasonable to expect the deformation behaviour and associated failure of micro-bumps is controlled by the properties of the IMCs. This has been implicitly observed in a previous study on the dimension effect on the tensile strength of solder joints that as the ratio between solder thickness and width decrease, the shear strength increases and mixed brittle and ductile fracture occurs [172]. In [172], the threshold thickness of solder is around 800 μm, which is significantly thicker than that in micro-bumps. Obviously, it is reasonable to conclude the deformation of micro-bumps in 3D ICs is likely to be of a brittle mode and controlled by IMCs. Because of the high volume fraction of IMCs, their phase transformation can induce higher internal strain and stress, which is undesirable for the integrity of micro-bumps. Because of the increased current density and resultant operating temperature of micro-bumps, the mechanical properties of Cu_6Sn_5 at high temperature, and their variation under high TM and EM are both critical. Intensive research has been recently reported recently to characterize the thermal or electric gradient induced material migration and associated microstructure variation of micro-bump in 3D ICs; however, it is still a challenge to stabilize the microstructure and improve the reliability of a micro-bump.

7. Summary

The electronic packaging industry is being forced, through the commercial need to satisfy Moore's rule and legislation, to increase the density of electronic packages and miniaturise circuit boards while simultaneously eliminating Pb from their existing products. This is occurring in an environment where electronic devices contain more and more complex dense circuitry and advanced manufacture techniques such as wafer-level packaging become more commonly employed in mass production. In soldered connections in electronic packages, Cu_6Sn_5 intermetallics account for a large and increasing fraction of the microstructure, and as such, offer the key to improving joint reliability. It is only by thoroughly

understanding the properties of this important intermetallic that significant advances can be made in the fabrication of new lead-free micro/nano electronic joints that offer increased reliability and that can be confidently used over an extended range of operating conditions for high density data storage, compact portable electronic devices and novel transportation and medical applications. Research reviewed in this paper has been focused on that related to developing an in-depth understanding of the properties of Cu_6Sn_5. In this paper the research on the properties of Cu_6Sn_5, collated from diverse disciplines, is summarised. In doing so, a platform where the properties of Cu_6Sn_5 can be readily correlated with each other has been established and how the properties of Cu_6Sn_5 affect the integrity of a soldered joint has been emphasized.

Previous researchers have used a variety of techniques to understand the relationship between fundamental crystallography, manufacturing parameters, solder alloy composition and the resulting properties of the interfacial intermetallics and although remarkable progress has been achieved, there are still questions to be answered, including the following:

1) The crystal structure and phase transformation of Cu_6Sn_5 have been extensively investigated with consideration of the effects of alloying elements; however, some questions are yet to be answered. Firstly, the crystal structure of newly indexed monoclinic phase η^{4+1}, was obtained from a high-purity stoichiometric sample rather than the Cu_6Sn_5 in a solder joint [21]. This is important because this newly characterised monoclinic phase is expected to be the one formed at the solder/substrate interface. In addition, the stabilization effect of the doping elements was only reported after a relatively short aging process; knowledge on the segregation of doping elements and the kinetics of stabilized Cu_6Sn_5 during elongated aging treatment is important in order to improve the service reliability of solder joints. Lastly, the effects of other alloying elements such as Co and Mn, as well as effects of combinations of alloying elements, on the phase transformation of Cu_6Sn_5 are unknown, but readily obtained through a TEM or X-ray diffraction study.
2) Cu_6Sn_5 plays an important role in the solidification of Sn-Cu and Sn-Ag-Cu alloys. This is especially true for Sn-Cu alloys, for which the Cu_6Sn_5 is the leading phase even on the hypo-eutectic side and affects the subsequent eutectic solidification. The effects of alloying elements on the coarsening

kinetics of Cu_6Sn_5, as well as Ag_3Sn, are of particular importance because the release of thermal stress in a solder joint is often associated with the coarsening of precipitating phases and recrystallization of eutectic or primary Sn-rich phase. Moreover, the solidification of Cu_6Sn_5 in Sn-Ag-Cu alloy has not been studied as comprehensively as the Sn-Cu alloy, presumably due to the complication in determining the solidification path in a non-eutectic ternary system.

3) In this article, the role of Cu_6Sn_5 in the wetting of molten solder on the substrate was not included. The wetting of molten solders on a solid substrate was commonly studied by making a non-reactive assumption that the interface reaction has no effect on the wetting process. However, it has been recognised that the formation of interfacial Cu_6Sn_5 significantly improves the wettability of SnPb alloys [12, 16]. A reactive model based on the investigations of wetting molten metals on ceramic or metal substrates was proposed as the intermetallic layers grow somewhere in front of the edge of the liquid droplets [182, 183]. Therefore, the molten solders wet the intermetallic layer. Experimental work has clearly demonstrated the effects of interfacial formation of Cu_6Sn_5 on the wetting kinetics of molten solders [16], however highly accurate data is needed to describe the atomic transportation process during reactive wetting, especially at the very early stage.

4) In Section 4, the interface reaction of Cu_6Sn_5 was mainly discussed according to the type of substrates in conventional solder joints or in the micro-bumps in 3D ICs. Compared to the intensive research on the formation of Cu_6Sn_5 and Cu_3Sn in these two arrangements, the formation of Cu_6Sn_5 in sandwich structure was not discussed in detail. As the size of conventional BGA balls gradually scales down, not only the crystal orientation of grains in the substrate, but also the dissolution of substrate materials affect the formation on both sides of a solder joints [184, 185]. Systematic study on the effects of the size and geometry of solder joints on the interface formation of IMCs and microstructure of solder joints, especially those with a size approaching 100 μm, is important for the development of highly reliable solder alloys and understanding the failures of solder joints, but this information is still scarce in the literature.

5) The effect of temperature on the mechanical properties of Cu_6Sn_5 has been recently investigated. However, as mentioned in Section 5, inconsistent results have been reported and more research is

needed to characterise the mechanical properties, especially the creep of Cu_6Sn_5 at elevated temperature. Moreover, it has been reported that the increased current through micro-bumps results in the decomposition of Cu_6Sn_5 [186]. Whether and how the electrical current affects the Cu_6Sn_5 crystal structure and hence the mechanical properties requires more detailed research.

Acknowledgement

This research was conducted under an international cooperative research program between the University of Queensland (UQ), Australia and Nihon Superior Company, Japan, and Australian Research Council Linkage projects (LP100200250 and LP140100485). D. Mu acknowledges the financial support received in the form of an Australian Postgraduate Award (APA). The authors thank Dr. G. Zeng in the University of Queensland for stimulating discussion and comments.

Table1: Reported Crystal structures of Cu_6Sn_5

Phase	Structure	a (Å)	b (Å)	c (Å)	α	β	γ
η-Cu_6Sn_5 [16]	Hexagonal	4.190	b=a	5.086	90°	β=α	120°
η'-Cu_6Sn_5 [16]	Monoclinic	11.022	7.282	9.827	90°	98.84°	γ=α
η^6-Cu_6Sn_5 [8]	Monoclinic	12.60	7.27	10.20	90°	90°	γ=α
η^8-Cu_6Sn_5 [8]	Monoclinic	9.83	7.27	c=a	90°	62.5	γ=α
η^{4+1}-Cu_6Sn_5 [19]	Monoclinic	92.241	7.311	9.880	90°	118.95°	γ=α

Table 2: Elastic modulus and hardness of Cu_6Sn_5 at room temperature

IMCs	Young's modulus (GPa)	Hardness (GPa)	Reference
Cu_6Sn_5	91.7	3.6	[166]
	134±7	6.5±0.3	[187]
	144.9±1.5 to 125.0±6.8	5.62±0.35 to 6.27±0.30	[188]
	116.77±1.64	5.40±0.69	[141]
	59.0 to 115.1	2.44 to 6.67	[142]
	116.89±2.04 118.97 ± 1.93	6.35±0.20 6.45 ± 0.14	[143]
	112.3 ± 5.0	6.38 ± 0.21	[144] [10]
	124.16 to 129.38	7.31 to 6.84	[145]
	95.7 to 97.4	5.67 to 6.09	[146, 154]
	129.0± 4.0 to 133.9 ± 9.0	5.6± 2.1 to 4.8±1.9	[147]
	126.995±2.342 to 125.845±3.045 114.527±5.189 to125.845±3.045	6.47±0.156 to 6.824±0.104 6.222±0.08 to 6.749±0.147	[148]
	120.98±2.46 105.00±1.80	6.02±0.20 to 5.69±0.14	[150]
	115.5±4.1	n.a.	[169]
	130±9	6.67±0.43	[152]
	117±5	6.7±0.4	[153]
	126±2.4	7.24±0.09	[165]
	120	n.a.	[162]
	125.98	n.a.	[163, 189]
	93	n.a.	[137]

References

1. H. Y. Hsiao, C.M. Liu, H.W. Lin, T.C. Liu, C. L. Lu, Y.S. Huang, C. Chen, K.N Tu, Sci. 336 (2012) 1007-1010.
2. K.N. Tu, Microelectron. Reliab., 51 (2011) 517-523.
3. Y.C. Chan, D. Yang, Prog. Mater. Sci., 55 (2010) 428-475.
4. M. Abtew, G. Selvaduray, Mater. Sci. Eng. R, 27 (2000) 95-141.
5. K. Suganuma, Current Opinion in Solid State & Materials Science 2001 (5) 55-64.
6. K. Zeng, K.N Tu, Mater. Sci. Eng. R, 2002 (38) 55-105.
7. N. Chawla, Inter. Mate. Rev., 54 (2009) 368-384.
8. W.M. Chen, T.L. Yang, C.K. Chung, C.R. Kao, Scrip. Mater., 65 (2011) 331-334.
9. A. K. Larsson, L. Stenberg, S. Lidin, Acta Crystallogr. B 50 (1994) 636-643.
10. X. Deng, N. Chawla, K.K. Chawla, M. Koopman, Acta. Mater., 52 (2004) 4291-4303.
11. B. Drevet, D. Camel, M. Dupuy, J.J. Favier, Acta. Mater., 44 (1996) 4071-4084.
12. H. Kim, K.N. Tu, Phys. Rev. B, 53 (1996) 16027.
13. A. Gusak, K.N. Tu, Phys. Rev. B, 66 (2002) 115403.
14. R. Gagliano, G. Ghosh, M. Fine, J. Electron. Mater., 31 (2002) 1195-1202.
15. G. Ghosh, M. Asta, J. Mater. Res., 20 (2005) 3102-3117.
16. A. Wedi, D. Baither, G. Schmitz, Scrip. Mater., 64 (2011) 689-692.
17. H. Okamoto, Phase diagrams of dilute binary alloys. ASM International (2002), 243.
18. G. Zeng, S.D. McDonald, J. Read, Q.F. Gu, K. Nogita, Acta Mater., 69 (2014) 135-148.
19. A. Gangulee, G. Das, M. Bever, Metall. Trans., 4 (1973) 2063-2066.
20. K. Nogita, C. Gourlay and T. Nishimura, JOM, 61 (2009) 45-51.
21. Y.Q. Wu, J.C. Barry, T. Yamamoto, Q.F. Gu, S.D. McDonald, S. Matsumura, H. Huang, K. Nogita, Acta Mater., 60 (2012) 6581-6591.
22. K.K.Wang, D. Gan, K.C. Hsieh, Thin Solid Films, 519 (2010) 1380-1386.
23. K.K. Wang, D. Gan, K.C. Hsieh, S.Y. Chiou, Thin Solid Films, 518 (2010) 1667-1674.
24. X.J. Liu, R. Kainuma, C.P. Wang, I. Ohnuma, K. Ishida, Metall. Mater. Trans. A, 35 (2004) 1641-1654.
25. M. Li, Z. Zhang, J. Kim, App. Phys. Lett., 98 (2011) 201901.
26. K. Nogita, C.M. Gourlay, S.D. McDonald, Y.Q. Wu, J. Read, Q.F. Gu, Scrip. Mater., 65 (2011) 922-925.
27. Z.B. Luo, L. Wang, Q.Q. Fu, C.Q. Cheng, J. Zhao, J. Mater. Res., 26 (2011) 1468-1471.
28. K. Nogita, T. Nishimura, Scrip. Mater., 59 (2008) 191-194.
29. U. Schwingenschlögl, C. Di Paola, K. Nogita, C. Gourlay, App. Phys. Lett., 96 (2010) 061908-061908-3.
30. Y.Q. Wu, S.D. McDonald, J. Read, H. Huang, K. Nogita, Scrip. Mater., 68 (2012) 595-598.
31. C.H. Lin, S.W. Chen, C.H. Wang, J. Electron. Mater., 31 (2002) 907-915.
32. C. Yu, J.Y. Liu, H. Lu, P.L. Li, J.M. Chen, Intermetallics, 15 (2007) 1471-1478.
33. C.Y.Yu, J.G. Duh, Scrip. Mater., 65 (2011) 783-786.
34. W.Q. Shao, C.Y. Yu, W.C. Lu, J.G. Duh, S.O. Chen, Mater. Lett., 93 (2013) 300-303.
35. Y. Yang, Y.Z. Li, H. Lu, C. Yu, J.M. Chen, Comp. Mater. Sci., 65 (2012) 490-493.
36. G. Zeng, S.D McDonald, Q.F. Gu, K. Nogita, J. Mater. Res., 27 (2012) 2609.
37. S.Lidin, S.Y. Piao, Zeitschrift für anorganische und allgemeine Chemie, 635 (2009) 611-613.
38. G. Zeng, S.D. McDonald, Q.F. Gu, S. Suenaga, Y. Zhang, J.H Chen, K. Nogita, Intermetallics,43 (2013)85-98.
39. K. W. Moon, W. J. Boettinger, U. R. Kattner, F. S. Biancaniello, C. A. Handwerker, J. Electron. Mater., 29 (2000) 1122-1136.
40. U. Kattner, JOM, 54 (2002) 45-51.
41. T. Ventura, S. Terzi, M. Rappaz, A.K. Dahle, Acta Mater., 59 (2011) 1651-1658.
42. C. M.Gourlay, K.Nogita, A. K. Dahle,Y. Yamamoto, K. Uesugi, T. Nagira, M. Yoshiya, H. Yasuda, Acta. Mater., 59 (2011) 4043-4054.
43. E. Çadırlı, U. Böyük, S. Engin, H. Kaya, N. Maraşlı, A. Ülgen, J. Alloy. Compd., 486 (2009) 199-206.
44. C.C. Mardare, A.W. Hassel, Phys. Status. Solidi. A, 209 (2012) 825-831.
45. J.E. Spinelli, A. Garcia, Mater. Sci. Eng. A, 658 (2013) 195-201.
46. F.Y. Hung, T.S. Lui, L.H. Chen, N.T He, J. Alloy. Compd., 457 (2008) 171-176.
47. G. Zeng, S.B. Xue, L. Zhang, L.L. Gao, J. Mater. Sci. Mater. Electron., 22 (2011) 565-578.
48. T. Ventura, C.M. Gourlay, K. Nogita, T.Nishimura, M. Rappaz, A.K.Dahle, J. Electron. Mater., 37 (2008) 32-39.
49. C.M. Gourlay, K. Nogita, J. Read, A.K Dahle, J. Electron. Mater., 39 (2010) 56-69.
50. K. Nogita, J. Read, T.Nishimura, K. Sweatman, S. Suenaga, A.K. Dahle, Mater. Trans., 46 (2005) 2419.
51. T. Ventura, S. Terzi, M. Rappaz, A.K. Dahle, Acta Mater., 59 (2011) 4197-4206.
52. M. Felberbaum, T. Ventura, M. Rappaz, A.K. Dahle, JOM, 63 (2011) 52-55.
53. F.J. Wang, X. Ma, Y. Qian, Scrip. Mater., 53 (2005) 699-702.
54. S.J. Kim, K.S. Kim, S.S. Kim, K. Suganuma, J. Electron. Mater., 38 (2009) 266-272.
55. G. Zeng, M.D. McDonald, C.M. Gourlay, K. Uesugi, Y. Terada, H. Yasuda, K. Nogita,, Metall. Mater. Trans. A, 45 (2014) 918-926.
56. C.M.L. Wu, D.Q. Yu, C.M.T. Law, L. Wang, J. Electron. Mater., 31 (2002) 928-932.
57. P. Sun, C. Andersson, X.C. Wei, Z.N. Cheng, D.K. Shangguan, J. Liu, Mater. Sci. Eng. B, 135 (2006) 134-140.
58. I.E. Anderson, J.C. Foley, B.A. Cook, J. Harringa, R.L. Terpstra, O. Unal, J. Electron. Mater., 30 (2001) 1050-1059.

59. G. Zeng, S. McDonald, K. Nogita, Microelectron. Reliab., 52 (2012) 1306-1322.
60. K. Suganuma, S.J. Kim, K.S. Kim, JOM, 61 (2009) 64-71.
61. K. Nogita, M. Greaves, M., Guymer, B. Walsh, J. Kennedy, T. Nishimura, ICEP-2010 International Conference on Electronics Packaging. 2010: Sapporo, Japan.
62. S.D. McDonald, K. Nogita, J. Read, T. Ventura, T. Nishimura, J. Electron. Mater., 42 (2012) 256-262.
63. J.W. Xian, S.A. Belyakov, T.B. Britton, C.M. Gourlay, J. Alloy. Comp., 619 (2015) 345-355.
64. J. Keller, D. Baither, U. Wilke, G. Schmitz, Acta. Mater., 59 (2011) 2731-2741.
65. K.E. Yazzie, H. Fei, H. Jiang, N. Chawla, Acta Mater., 60 (2012) 4336-4348.
66. C.M. Miller, I.E. Anderson, J.F. Smith, J. Electron. Mater., 23 (1994) 595-601.
67. M. Loomans, M. Fine, Metall. Mater. Trans. A, 31 (2000) 1155-1162.
68. D. Lewis, S. Allen, M. Notis, A. Scotch, J. Electron. Mater., 31 (2002) 161-167.
69. J.Y. Park, C.U. Kim, T. Carper, V. Puligandla, J. Electron. Mater., 32 (2003) 1297-1302.
70. S.L. Allen, M.R. Notis, R.R. Chromik, R.P Vinci, J. Mater. Res., 19 (2004) 1417-1424.
71. S.L. Allen, M.R. Notis, R.R. Chromik, R.P Vinci, D.J. Lewis, R. Schaefer, J. Mater. Res., 19 (2004) 1425-1431.
72. L. Snugovsky, D.D. Perovic, J.W. Rutter, Powder Metall., 48 (2005) 193-198.
73. L. Snugovsky, P. Snugovsky, D.D. Perovic, J.W. Rutter, Mater. Sci. Tech., 21 (2005) 61-68.
74. T.R. Bieler, H.R. Jiang, L.P. Lehman, T.Kirkpatrick, E.J. Cotts, B. Nandagopal, IEEE Trans. Comp. Packag. Tech., 31 (2008) 370-381.
75. L.L. Gao, S.B, Xue, L. Zhang, Z. Sheng, F. Ji, W. Dai, S.J. Yu, G. Zeng, Microelectron. Eng., 87 (2010) 2025-2034.
76. M.A. Dudek and N. Chawla, Metall. Mater. Trans. A, 41 (2010) 610-620.
77. T. Laurila, V. Vuorinen, J.K. Kivilahti, Mater. Sci. Eng. R 49 (2005) 1-60.
78. T. Laurila, V. Vuorinen, M. Paulasto-Kröckel, Mater. Sci. Eng. R 68 (2010) 1-38
79. B.J. Lee, N.M. Hwang, H.M. Lee, Acta Mater., 45 (1997) 1867-1874.
80. R. Lord, A. Umantsev, J. App. Phys., 98 (2005) 063525-063525-11.
81. M. Park, R. Arróyave, Acta Mater., 58 (2010) 4900-4910.
82. K.N. Tu, A.M. Gusak, M. Li, J. App. Phys., 93 (2003) 1335-1353.
83. K.H. Prakash, T. Sritharan, Acta Mater., 49 (2001) 2481-2489.
84. M.Yang, M. Li, C. Wang, Intermetallics, 25 (2012) 86-94.
85. J. Gorlich, G. Schmitz, K.N. Tu, App. Phys. Lett., 86 (2005) 053106-053106-3.
86. M. Schaefer, R.A. Fournelle, J. Liang, J. Electron. Mater., 27 (1998) 1167-1176.
87. C.K. Chung, J.G. Duh, C.R. Kao, Scrip. Mater., 63 (2010) 258-260.
88. S. Bader, W. Gust, H. Hieber, Acta Metall. Mater., 43 (1995) 329-337.
89. R.A. Gagliano, M.E. Fine, J. Electron. Mater., 32 (2003) 1441-1447.
90. R.A. Gagliano, M.E. Fine, JOM, 53 (2001) 33-38.
91. M.S. Park, R. Arróyave, Acta Mater., 60 (2012) 923-934.
92. H.F.Zou, H.J. Yang, Z.F. Zhang, Mater. Chem. Phys., 131 (2011) 190-198.
93. J.F. Li, P. Agyakwa, C. Johnson, Acta Mater., 59 (2011) 1198-1211.
94. Y. Takaku, X.J. Liu, I. Ohnuma, R. Kainuma, K. Ishida, Mater. Trans., 45 (2004) 646-651.
95. L. Qu, N. Zhao, H.J Zhao, M.L. Huang, H.T. Ma, Scrip. Mater., 72 (2014) 43-46.
96. P.J. Shang, Z.Q. Liu, X.Y. Pang, D.X. Li, J.K. Shang, Acta Mater., 57 (2009) 4697-4706.
97. K.N. Tu, Acta Metall., 21 (1973) 347-354.
98. K.N. Tu, Mater. Chem. Phys., 46 (1996) 217-223.
99. K.N.Tu, R.D. Thompson, Acta Metall., 30 (1982) 947-952.
100. X. Deng, G. Piotrowski, J.J. Williams, N. Chawla, J. Electron. Mater., 32 (2003) 1403-1413.
101. M. Yang, H.T. Chen, X. Ma, M.Y. Li, Y. Cao, J.Y. Kim, J. Mater. Sci., 49 (2014) 3652-3664.
102. J.O. Suh, K.N. Tu, G.V. Lutsenko, A.M. Gusak, Acta Mater., 56 (2008) 1075-1083.
103. M.Yang, M. Li, J. Kim, Intermetallics, 31 (2012) 177-185.
104. J.W. Yoon, Y.H. Lee, D.G. Kim, H.B. Kang, S.J. Suh, C.W. Yang, C.B. Lee, J.M. Jung, C.S. Yoo, S.B. Jung, J. Alloy. Comp., 381 (2004) 151-157.
105. H. Nishikawa, J. Piao, T. Takemoto, J. Electron. Mater., 35 (2006) 1127-1132.
106. J.W.Yoon, S.B. Jung, Surf. Coat. Tech., 200 (2006) 4440-4447.
107. D. Mu, H. Yasuda, H. Huang, K. Nogita, J. Alloy. Comp., 56 (2012) 38-46.
108. T.Y. Lee, W.J. Choi, K.N. Tu, J.W. Jang, S.M. Kuo, J.K. Lin, D.R. Frear, K. Zeng, J.K. Kivilahti, J. Mater. Res., 17 (2002) 291-301.
109. M.G. Cho, Y.S.Park, S.K. Seo, K.W. Paik, H.M. Lee, IEEE Trans. Comp. Packag. Manu. Tech., 1 (2011) 1939-1946.
110. X.Y. Liu, M.L. Huang, Y.H. Zhao, C.M.L. Wu, L. Wang, J. Alloy. Comp., 492 (2010) 433-438.
111. J.C. Gong, C.Q. Liu, P.P. Conway, V.V. Silberschmidt, Acta Mater., 56 (2008) 4291-4297.
112. M.Y Li, M. Yang, J. Kim, Mater. Lett., 66 (2012) 135-137.
113. J.C. Gong, C.Q. Liu, P.P. Conway, V.V. Silberschmidt, Scrip. Mater., 60 (2009) 333-335.
114. T. Laurila, J. Hurtig, V. Vuorinen, J.K. Kivilahti, Microelectron. Reliab., 49 (2009) 242-247.
115. H.Yu, V. Vuorinen, J. Kivilahti, IEEE Trans. Electron. Packag. Manu., 30 (2007) 293-298.
116. J.W. Yoon, S.W. Kim, S.B. Jung, J. Alloy. Comp., 415 (2006) 56-61.
117. H. Yu, V. Vuorinen, J. Kivilahti, J. Electron. Mater., 36 (2007) 136-146.
118. Y.W.Wang, C.C. Chang, C.R. Kao, J. Alloy. Comp., 478 (2009) L1-L4.

119. G. Zeng, S.D. McDonald, D. Mu, Y. Terada, H. Yasuda, Q.F. Gu, K. Nogita, Intermetallics, 54 (2014) 20-27.
120. H. Tsukamoto, T. Nishimura, K. Nogita, Mater. Lett., 63 (2009) 2687-2690.
121. C.Y. Chou, S.W. Chen, Y.S. Chang, J. Mater. Res., 21 (2006) 1849-1856.
122. S.W. Chen, S.H. Wu, S.W. Lee, J. Electron. Mater., 32 (2003) 1188-1194.
123. J. Görlich, D. Baither, G. Schmitz, Acta Mater., 58 (2010) 3187-3197.
124. W. Chen, C. Ho, C. Kao, J. Mater. Res., 17 (2002) 263-266.
125. J.W. Yoon, S.-B. Jung, J. Alloy. Comp., 396 (2005) 122-127.
126. C.H. Wang, S.W. Chen, Acta Mater., 54 (2006) 247-253.
127. S.W. Chen, C.H. Wang, J. Mater. Res., 21 (2006) 2270-2277.
128. J.O. Suh, K.N. Tu, N. Tamura, App. Phys. Lett., 91 (2007) 051907-051907-3.
129. H. Zou, H. Yang, Z. Zhang, Acta Mater., 56 (2008) 2649-2662.
130. J.O. Suh, K.N. Tu, N. Tamura, J. App. Phys., 102 (2007) 063511-063511-7.
131. H.F. Zou, H.J. Yang, J. Tan, Z.F. Zhang, J. Mater. Res., 24 (2009) 2141-2144.
132. C. Chen, H.Y. Hsiao, Y.W. Chang, F.Y. Ouyang, K.N. Tu, Mater. Sci. Eng. R, 73 (2012) 85-100.
133. H. Gan, K.N. Tu, J. App. Phys., 97 (2005) 063514.
134. M.Y. Guo, C.K. Lin, C. Chen, K.N. Tu, Intermetallics, 29 (2012) 155-158.
135. N. Jiang, J.A. Clum, R.R. Chromik, E.J. Cotts, Scrip. Mater., 37 (1997) 1851-1854.
136. K.J. Wang, Y.C. Lin, J.G. Duh, C.Y. Cheng, J.J. Lee, J. Mater. Res., 25 (2010) 972-975..
137. W. Zhou, L. Liu, P. Wu, Intermetallics, 18 (2010) 922-928.
138. D. Mu, J. Read, Y.F. Yang, K. Nogita, J. Mater. Res., 26 (2011) 2660-2664.
139. K. Nogita, D. Mu, S.D. McDonald, J. Read, Y.Q. Wu, Intermetallics, 26 (2012) 78-85.
140. H.J. Albrecht, . in *Electron*. *Packag*. *Techn*., 2003 5th Conference (EPTC 2003). 2003. IEEE.
141. D. Li, C. Liu, P.P. Conway, Mater. Sci. Eng. A, 39 (2005) 95-103.
142. H. Rhee, J. Lucas, K. Subramanian, J. Mater. Sci. Mater. Electron., 13 (2002) 477-484.
143. P.F.Yang, Y.S. Lai, S.R. Jian, J. ChenR.S. Chen, Mater. Sci. Eng. A, 485 (2008) 305-310.
144. X. Deng, M. Koopman, N. Chawla, K.K. Chawla, Mater. Sci. Eng. A, 364 (2004) 240-243.
145. H. Tsukamoto, Z.G. Dong, H. Huang, T. Nishimura, Mater. Sci. Eng. B, 164 (2009) 44-50.
146. L. Xu, J.H. Pang, Thin Solid Films, 504 (2006) 362-366.
147. Y. Rosenthal, A. Stern, S.R. Cohen, D. Eliezer, Mater. Sci. Eng. A, 527 (2010) 4014-4020.
148. J.M. Song, B.R. Huang, C.Y. Liu, Y.S. Lai, Y.T. Chiu, T.W. Huang, Mater. Sci. Eng. A, 534 (2011) 53-59.
149. D. Mu, H. Huang, S.D. McDonald, J. Read, k. Noita, Mater. Sci. Eng. A, 566 (2013) 126-133.
150. D. Mu, H. Huang, K. Nogita, Mater. Lett., 86 (2012) 46-49.
151. L. Jiang, H. Jiang, N. Chawla, J. Electron. Mater., 41 (2012) 2083-2088.
152. V. Marques, C. Johnston, P. Grant, Acta Mater., 61 (2013) 2460-2470.
153. S. Lotfian, J.M Molina-Aldareguia, K.E. Yazzie, J. Llorca, N. Chawla, J. Electron. Mater., 42 (2013) 1085-1091.
154. L. Xu, J.H. Pang, J. Electron. Mater., 35 (2006) 2107-2115.
155. K. Nogita, H. Yasuda, C.M Gourlay, S. Suenaga, H. Tsukamoto, S.D. Mcdonald, A. Takeuchi, K. Uesugi, Y. Suzuki, Trans. Jpn. Inst. Electron. Packag. 3 (2010) 40-46.
156. Y. Hsiao, Y. Chuang, C. Liu, Scrip. Mater., 54 (2006) 661-664.
157. J. Yoon, S. Kim, S. Jung, J. Alloy. Comp., 385 (2004) 192-198.
158. F. Gao, T. Takemoto, J. Alloy. Comp., 421 (2006) 283-288.
159. K.C. Huang, K.-C., et al., J. Electron. Mater., 41 (2012) 172-175.
160. D. Mu, H. Tsukamoto, H. Huang, K. Nogita, Mater. Sci. Forum, 654 (2010) 2450-2454.
161. G.Zeng, D.K. Mu, S. D. McDonald, J. Read, H. Huang and K. Nogita, unpublished work.
162. N. Lee, V. Tan, and K. Lim, App. Phys. Lett., 88 (2006) 031913.
163. J. Chen, Y.S. Lai, P.F. Yang, C.Y. Ren, D.J. Huang, J. Mater. Res., 24 (2009) 2361-2372.
164. R. An, C.Q. Wang, Y.H. Tian, H.P Wu, J. Electron. Mater., 37 (2008) 477-482.
165. J.M. Song, C.W. Su, Y.S. Lai, Y.T. Chiu, J. Mater. Res., 25 (2010) 629-632.
166. J.P. Lucas, H. Rhee, F. Guo,K.N. Subramanian, J. Electron. Mater., 32 (2003) 1375-1383.
167. V.M.F. Marques, B. Wunderle, C. Johnston, P.S. Grant, Acta Mater., 61 (2013) 2471-2480.
168. G. Ghosh, J. Mater. Res., 19 (2004) 1439-1454.
169. L. Jiang, N. Chawla, Scrip. Mater., 63 (2010) 480-483.
170. Q. Zhang, J. Tan, Z. Zhang, J. Appl. Phys., 110 (2011) 014502-014502-4.
171. Q. Zhang, Z. Zhang, Scrip. Mater., 6 (2012) 289-292.
172. L. Yang, Q. Zhang, Z. Zhang, Scrip. Mater., 67 (2012) 637-640.
173. H. Zou, Z. Zhang, J. Mater. Res., 23 (2008) 1614-1617.
174. K.E.Yazzie H.X. Xie, J.J. Williams, and N. Chawla, Scrip. Mater., 66 (2012) 586-589.
175. J. Wang, H. Nishikawa, Microelectron. Reliab.,54 (2014) 1583-1591.
176. H.T. Lee, M.-H. Chen, Mater. Sci. Eng. A, 333 (2002) 24-34.
177. H. T. Lee, M.H. Chen, H. M. Jao, T. L. Liao, Mater. Sci. Eng. A, 358 (2003) 134-141.
178. S.M. Hayes, S.M., N. Chawla and D.R. Frear, Microelectron. Reliab., 43 (2009) 269-287.
179. W.Y. Chen, W. Tu, H.C. Chang, T.T. Chou, J.G Duh, Mater. Lett., 134 (2014) 184-186.
180. T. An, F. Qin, Microelectron. Reliab., 54 (2014) 932-938.
181. J. Shen, D.J. Zhai, Z.M. Cao, M. Zhao, Y.Y Pu,, J. Electron. Mater., 43 (2014) 567-578.

182. N. Eustathopoulos, Curr. Opin. Solid State Mater. Sci., 9 (2005) 152-160.
183. E. Saiz, A.P. Tomsia, Curr. Opin. Solid State Mater. Sci.,9 (2005) 167-173.
184. S.J. Wang, C.Y. Liu, Scrip. Mater., 55 (2006) 347-350.
185. Y.S. Huang, H.Y. Hsiao, C. Chen, K.N. Tu, Scrip. Mater., 66 (2012) 741-744.
186. C.K. Lin, C.M. Liu, C. Chen, Mater. Lett., 124 (2014) 261-263.
187. R.R Chromik, R.P. Vinci, S.L. Allen, M.r. Notis, J. Mater. Res., 18 (2003) 2251-2261.
188. G.Y. Jang, J.W. Lee, J.G. Duh, J. Electron. Mater., 33 (2004) 1103-1110.
189. J. Chen, Y.S. Lai, Microelectron. Reliab., 49 (2009) 264-268.

Figure

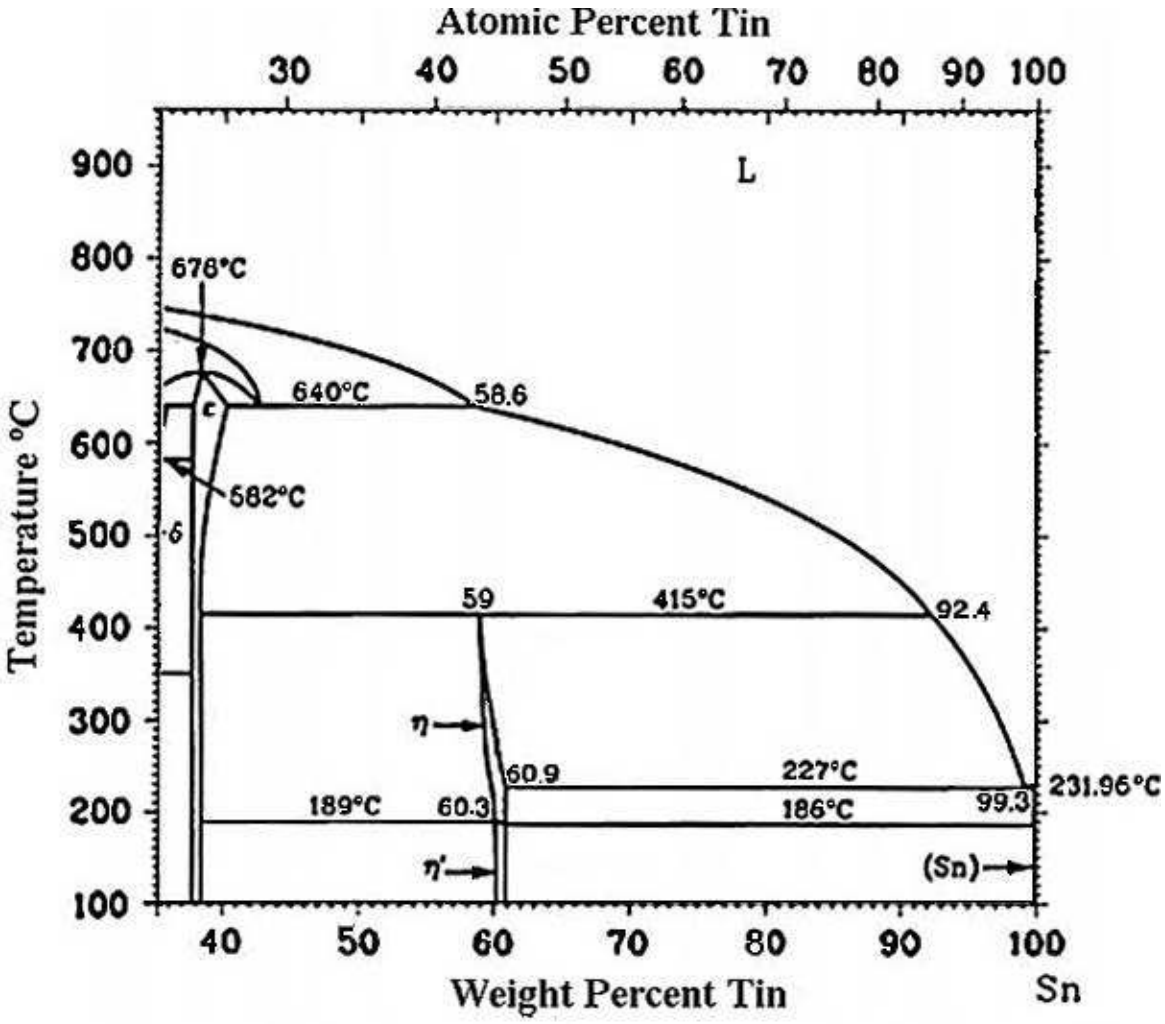

Figure 1: Sn-Cu phase diagram [17]

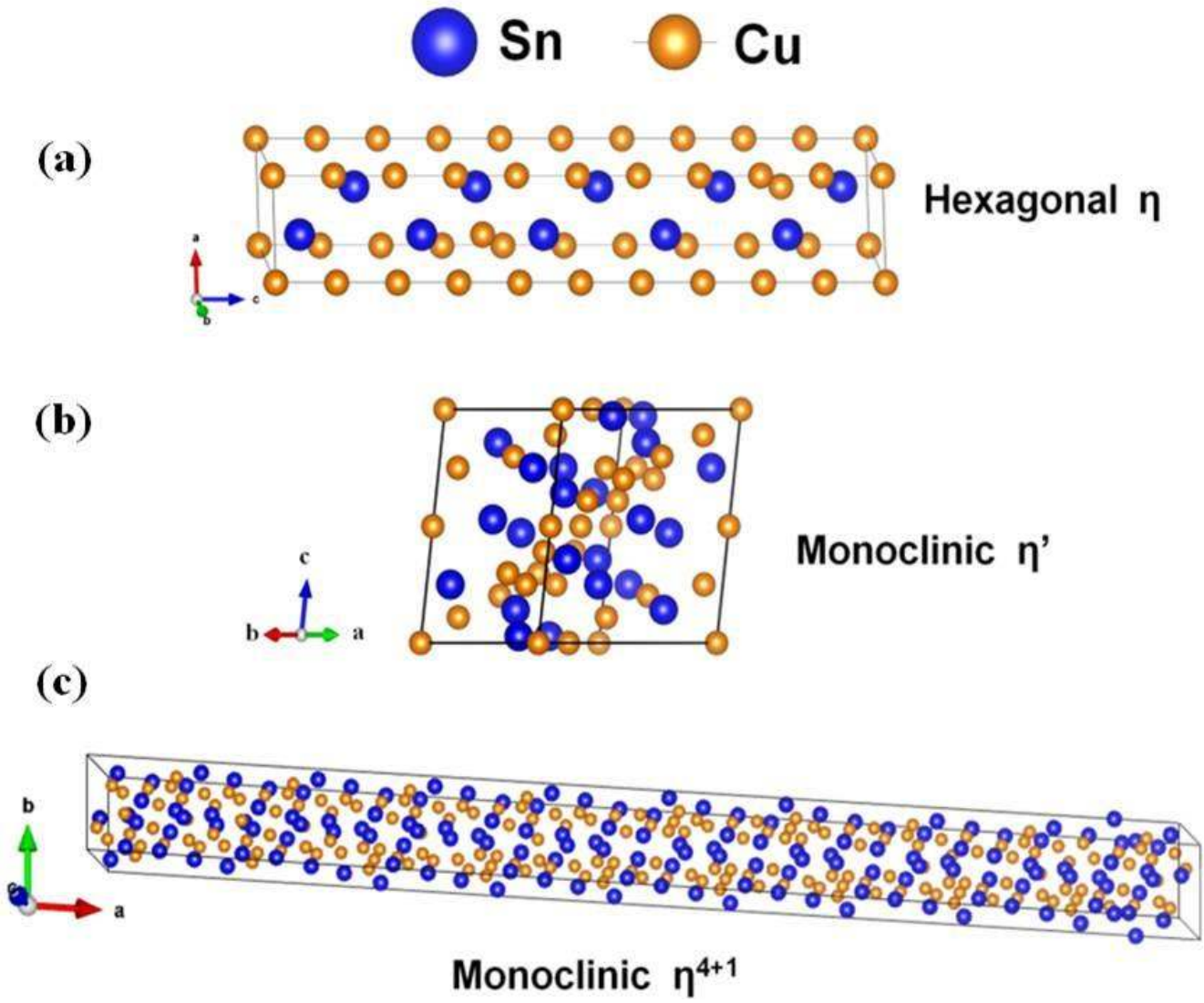

Figure 2: Crystal structures of Cu_6Sn_5 phases. Figures produced using the software VESTA [18].

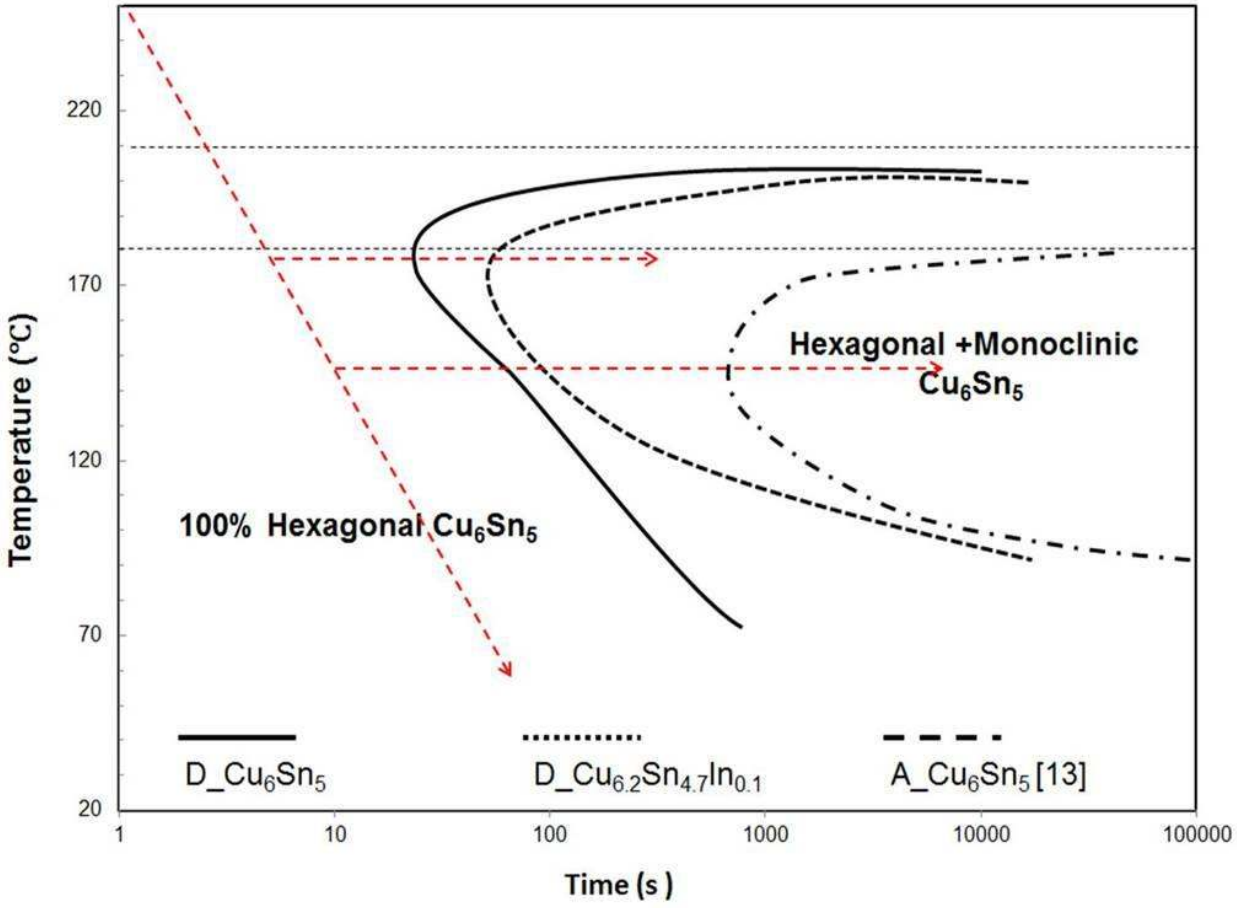

Figure 3: Time-temperature-transformation (TTT) curves of Cu_6Sn_5 obtained by synchrotron diffraction [18].

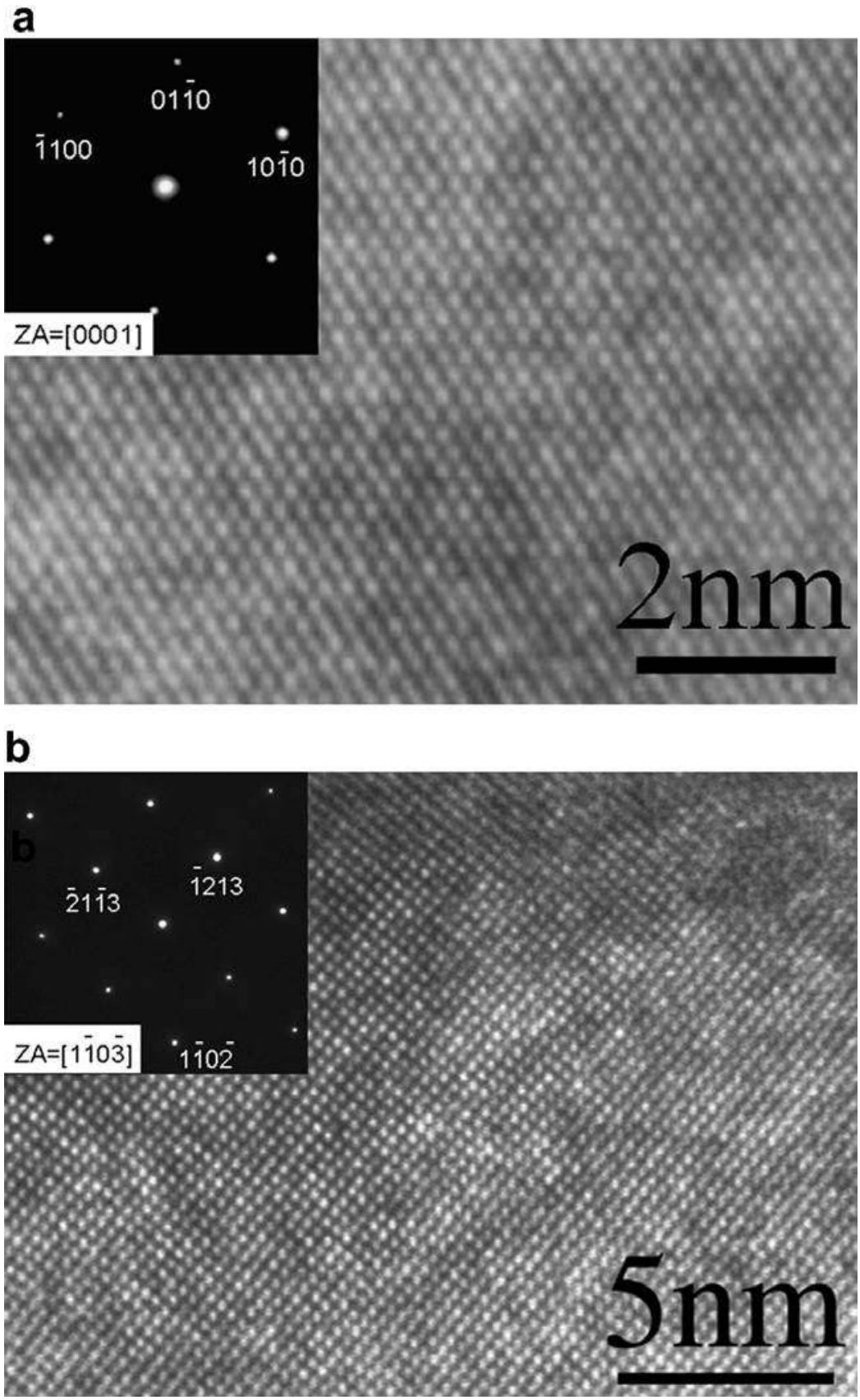

Figure 4: (a) Lattice image of $(Cu,Ni)_6Sn_5$ (IMC1) with 8.3 at.% Ni showing hexagonal structure with ED of the [0001] zone axis; (b) Lattice image $(Cu,Ni)_6Sn_5$ (IMC2) with 9 at.% Ni showing hexagonal structure with ED of the [1 $\bar{1}$ 0 $\bar{3}$] zone axis [28].

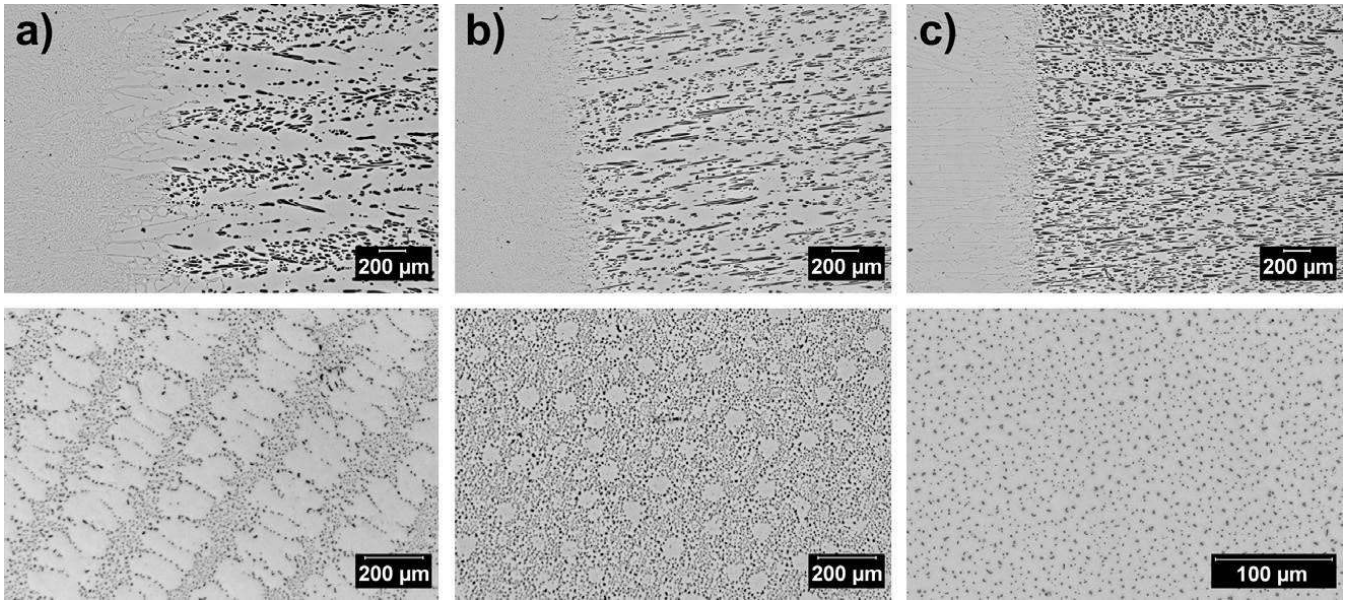

Figure 5: Longitudinal (top) and transverse (bottom) cross-sections of Bridgman samples solidified at 10 μm/s (a) off-eutectic structure with primary dendrites followed by a eutectic interface (Sn–0.5 Cu), (b) off-eutectic structure with primary cells followed by a eutectic interface (Sn–0.7 Cu) and (c) full eutectic structure with random distribution of Cu_6Sn_5 fibres (Sn–0.9 Cu) [41].

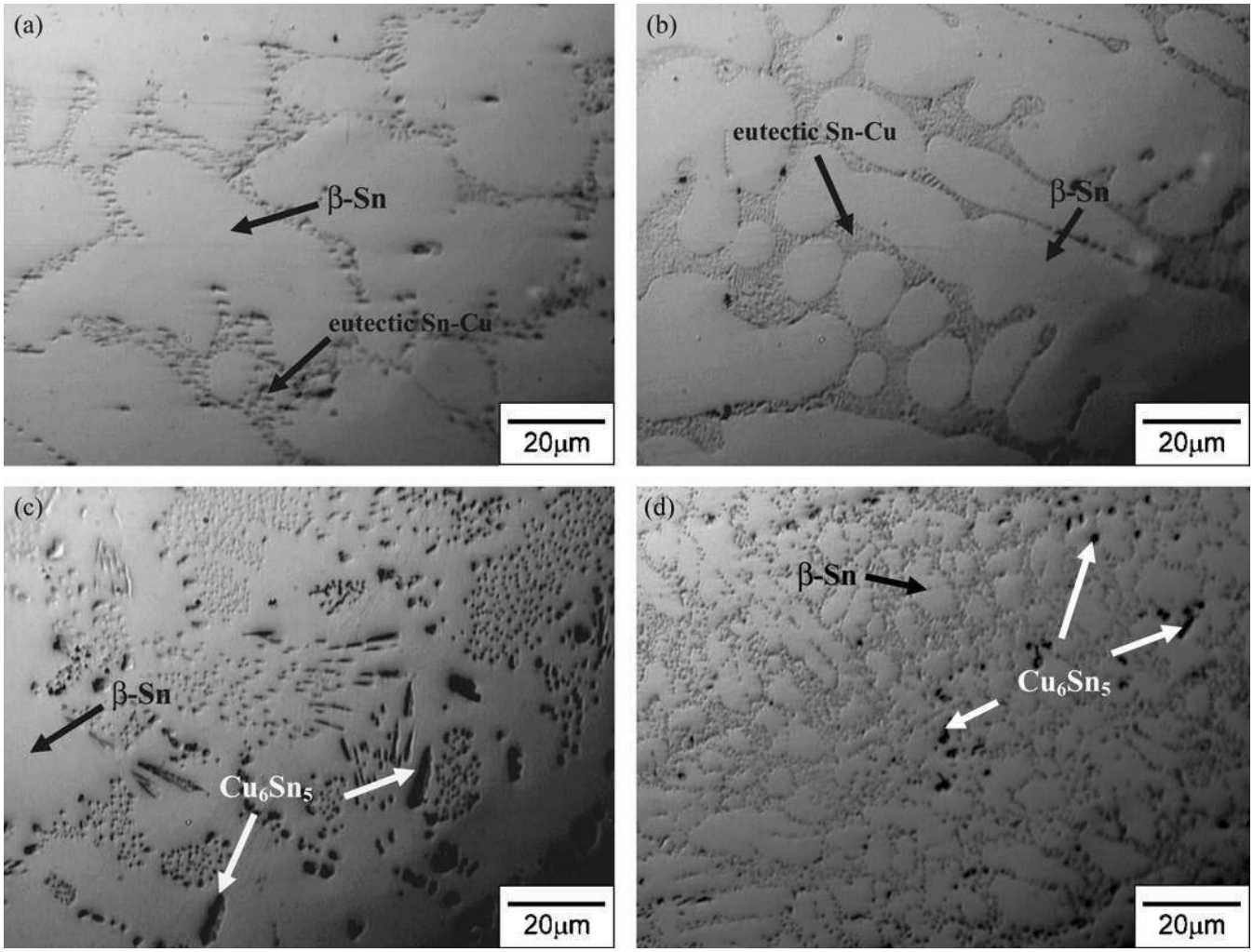

Figure 6: Air cooled microstructure of Sn- Cu solders: (a) 0.3, (b) 0.6, (c)1.3 and (d) 1.7 wt%Cu [46].

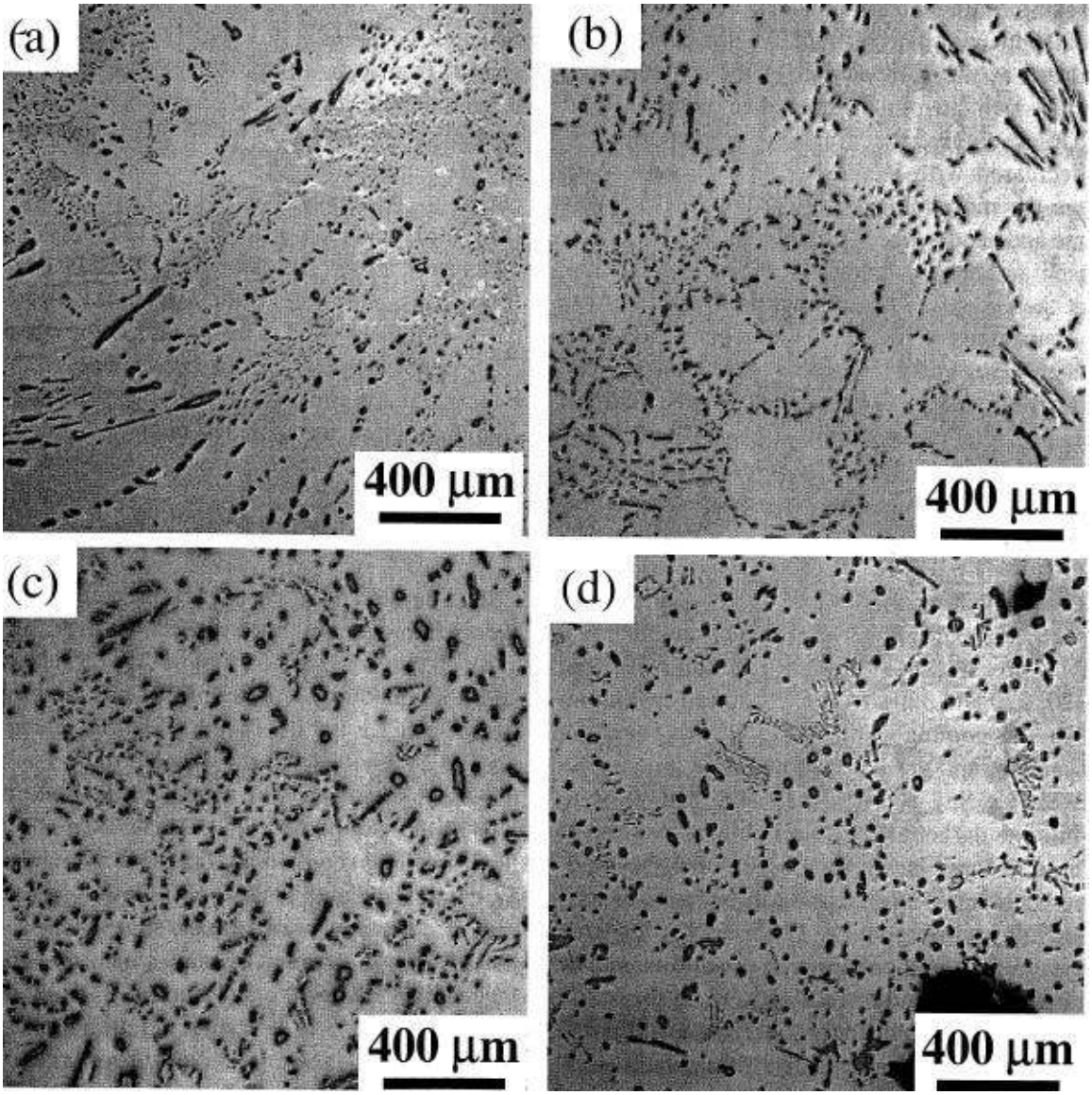

Figure 7: Optical micrographs of fully solidified samples. (a) Sn-0.7wt%Cu, (b) Sn-0.7wt%Cu-100 ppm Ni, (c) Sn-0.7wt%Cu-600 ppm Ni and (d) Sn-0.7Cu-1000 ppm Ni [50].

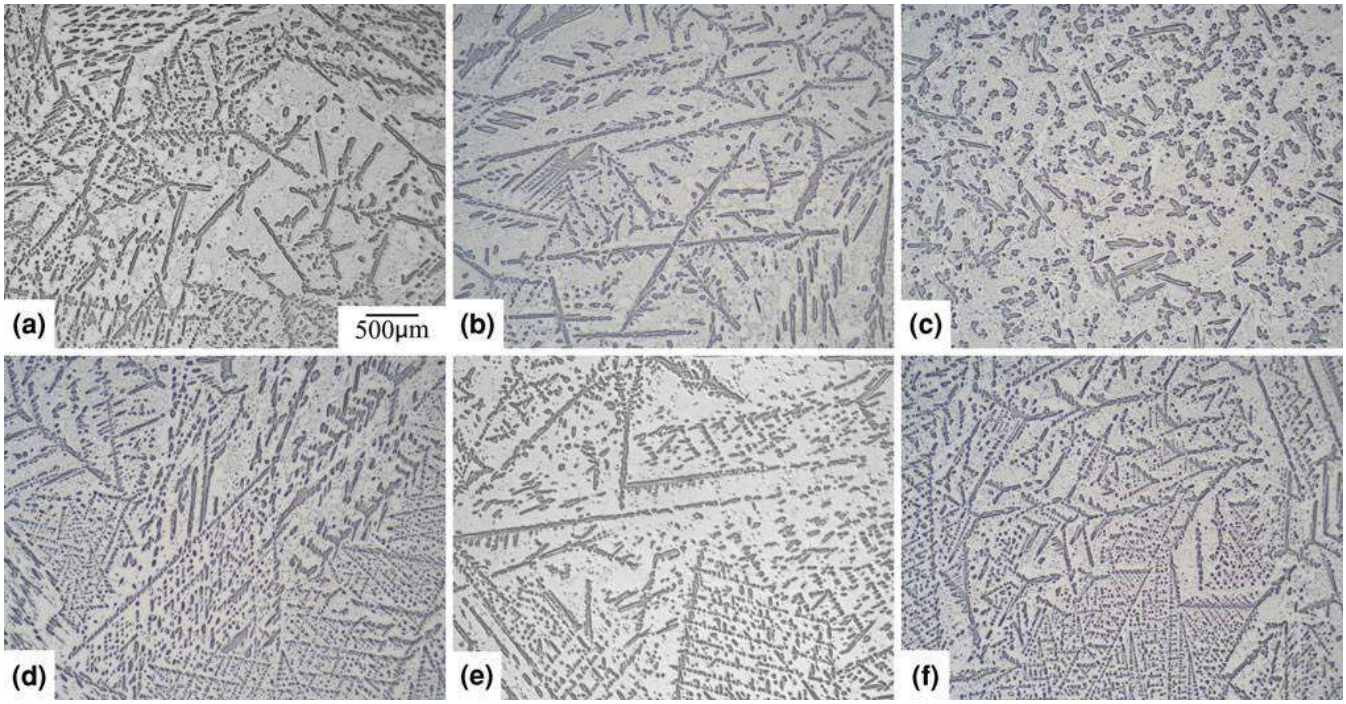

Figure 8: The effect of alloy additions on the morphology of primary Cu_6Sn_5: (a) base Sn-4Cu with no additions, (b) Sn-4Cu+500 ppm Ni, (c) Sn-4Cu + 500 ppm Al, (d) Sn-4Cu + 500 ppm Pb, (e) Sn-4 Cu + 500 ppm Ag, and (f) Sn-4Cu + 600 ppm Ge. Magnification is identical for all micrographs, and scale bar is shown in (a) [62].

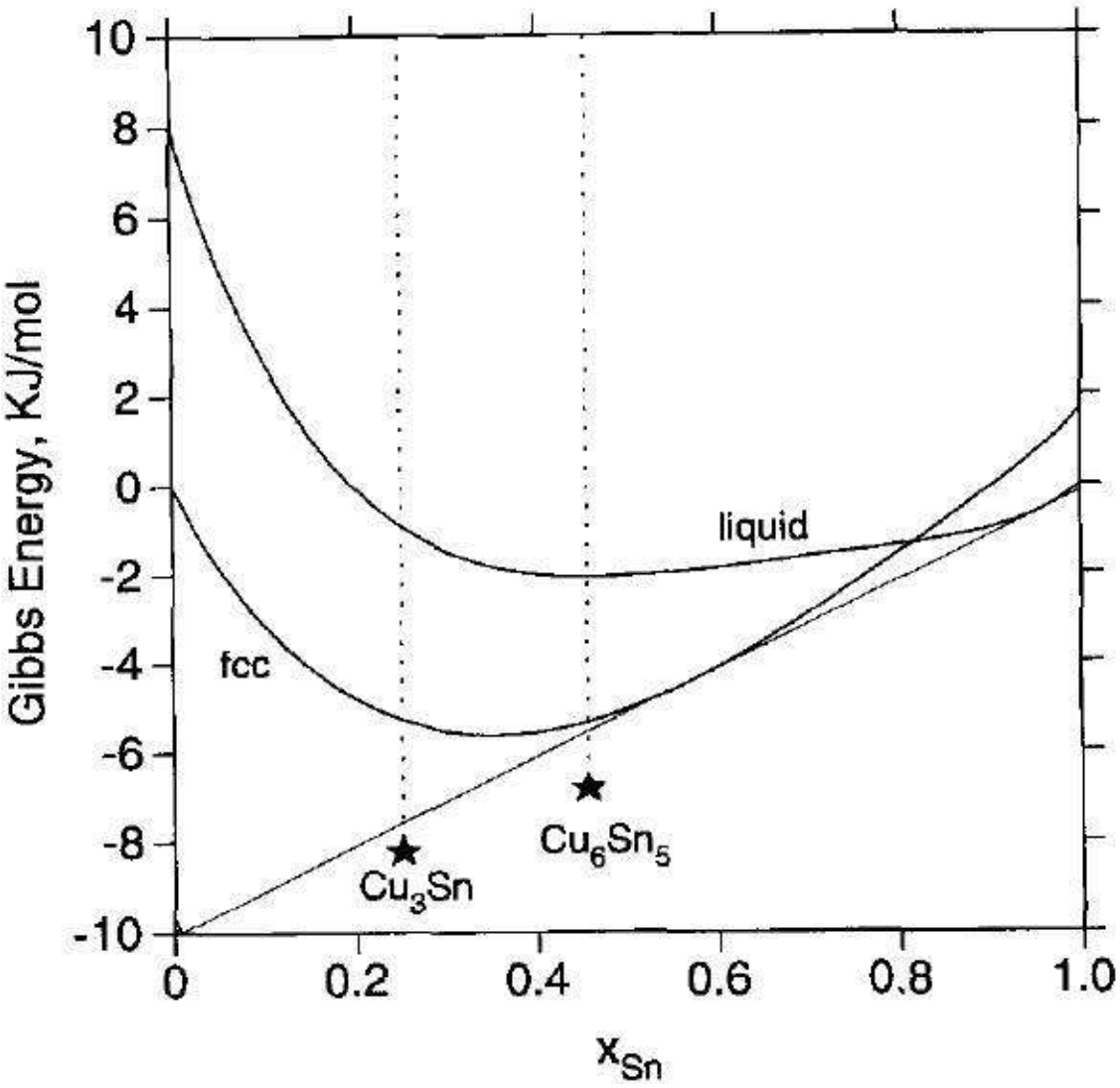

Figure 9: Illustration of driving forces of formation for Cu_3Sn and Cu_6Sn_5 under metastable equilibrium between f.c.c. and liquid at 250°C in Cu-Sn binary system. Thick lines are the Gibbs energy curves of f.c.c. and liquid, the thin line is the common tangent for the metastable equilibrium. The Gibbs energies of Cu_3Sn and Cu_6Sn_5 are denoted by "*". The vertical distances between the common tangent and the Gibbs energies of Cu_3Sn and Cu_6Sn_5 correspond to the driving forces of formation for both phases [79].

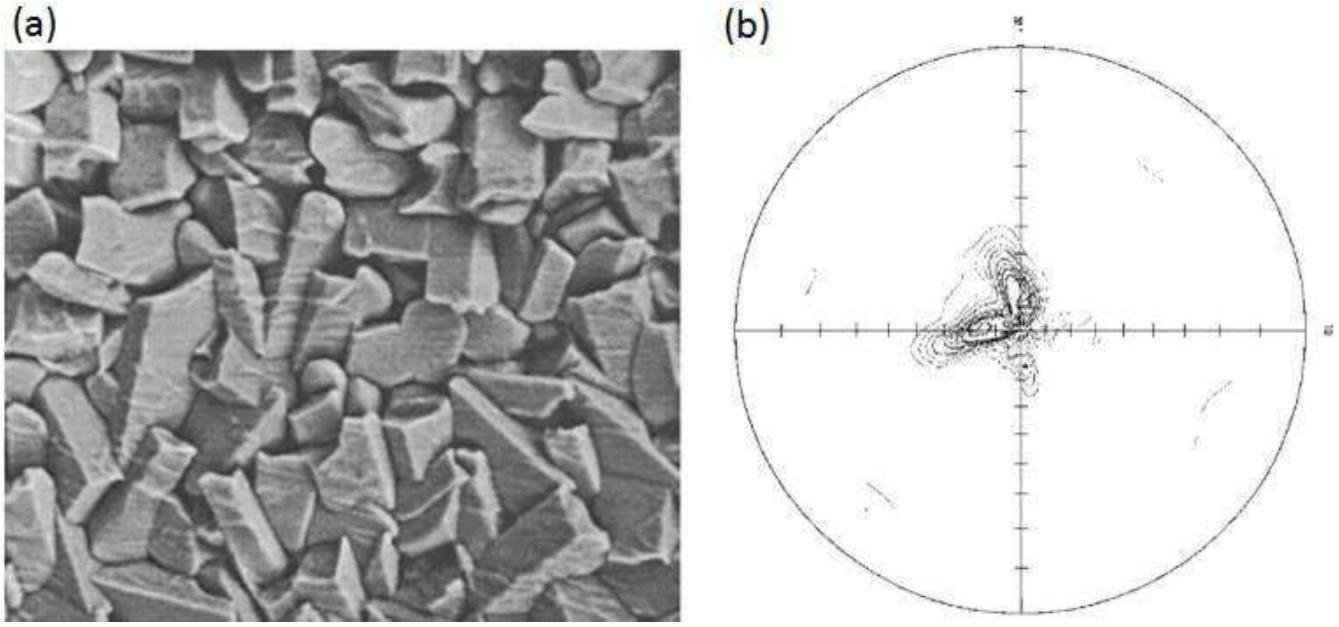

Figure 10: (a) SEM images of the top view of the morphology of Cu_6Sn_5 formed between Cu and pure Sn after etching the Sn away [82]. The Cu_6Sn_5 compound formed with pure Sn is highly faceted; (b) (101) pole figure of η phase film formed between Sn and Cu at 242 ^oC [83].

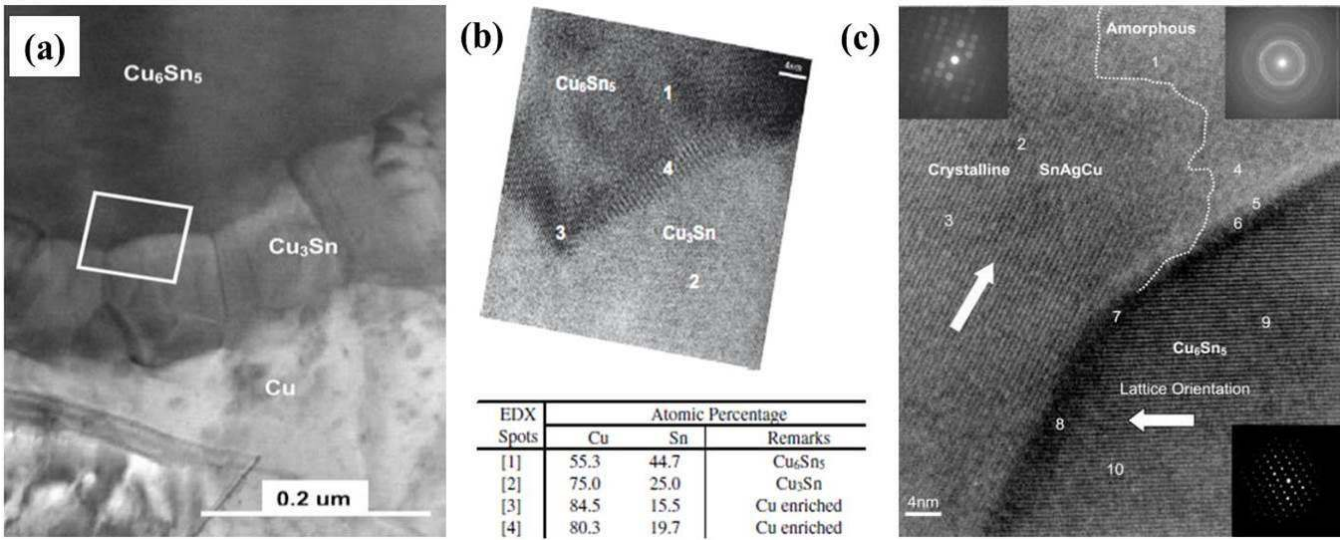

EDX Spots	Atomic Percentage		
	Cu	Sn	Remarks
[1]	55.3	44.7	Cu_6Sn_5
[2]	75.0	25.0	Cu_3Sn
[3]	84.5	15.5	Cu enriched
[4]	80.3	19.7	Cu enriched

Figure 11: (a) TEM micrograph showing thin columnar Cu_3Sn at the interface between Cu and Cu_6Sn_5. The thickness of Cu3Sn is <0.1 μm; (b) High-resolution TEM micrograph showing the interface between Cu_6Sn_5 and Cu_3Sn. This micrograph corresponds to the region within the white square in (a). Also shown are the spot compositions determined by EDX with a beam size of 1.2 nm; (c) High-resolution TEM micrograph showing the solder–Cu_6Sn_5 interface [87].

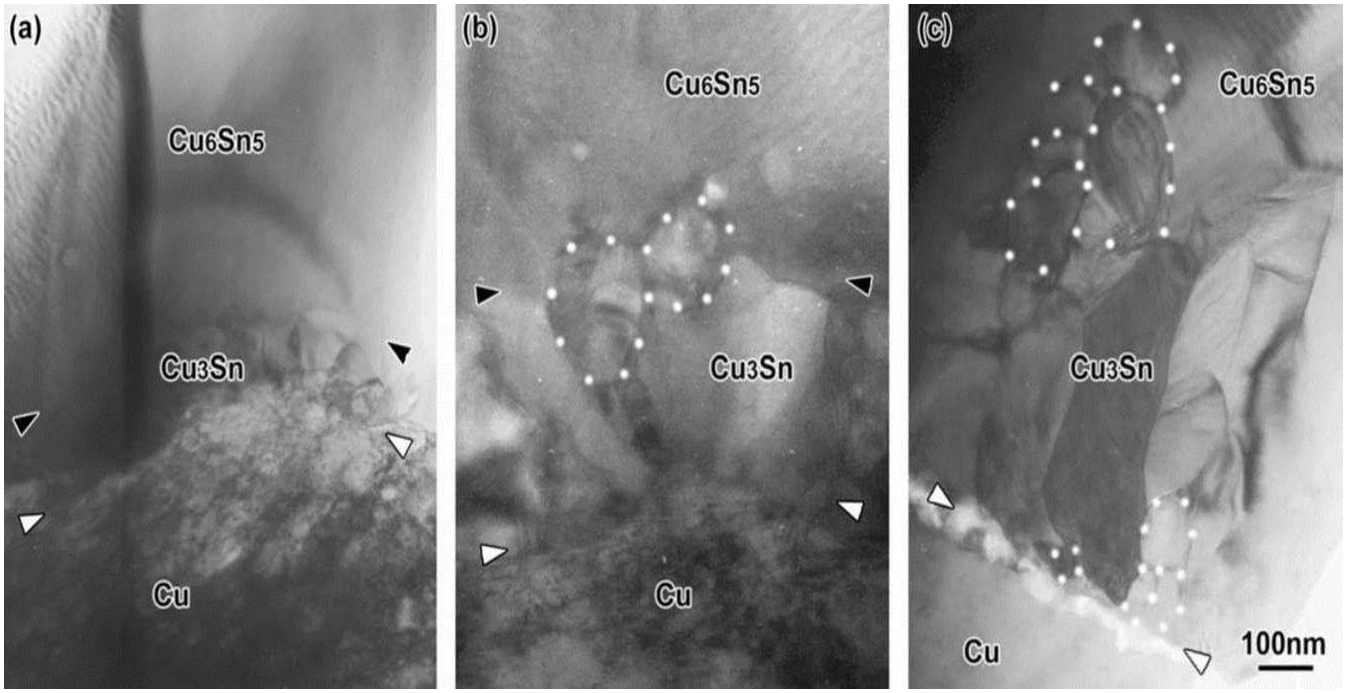

Figure 12: Interfacial BF images on polycrystalline Cu after (a) reflow, (b) aging for 24 h and (c) aging for 48 h at 393 K. Newly formed interfacial Cu_3Sn grains during solid state aging are marked with white dots [96].

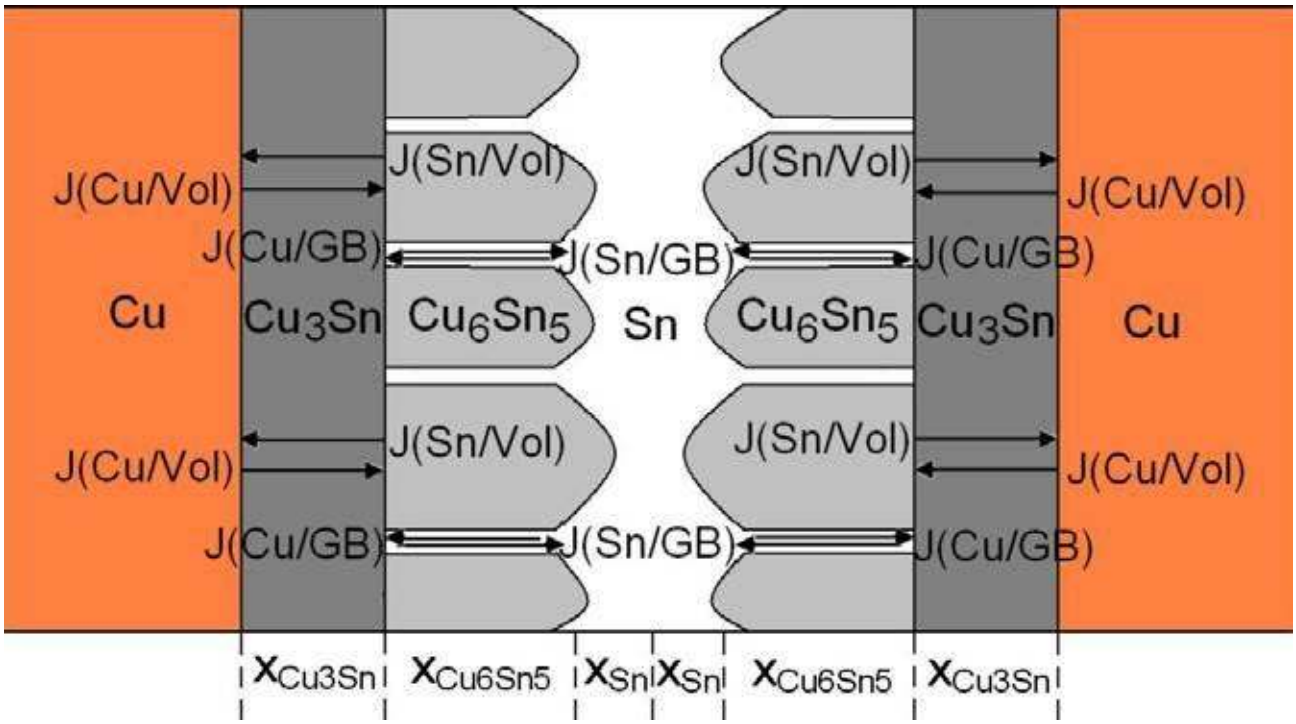

Figure 13: A schematic model of the possible fluxes due to interdiffusion in a Cu/Sn/Cu sample. Note that the different components are not to scale [93].

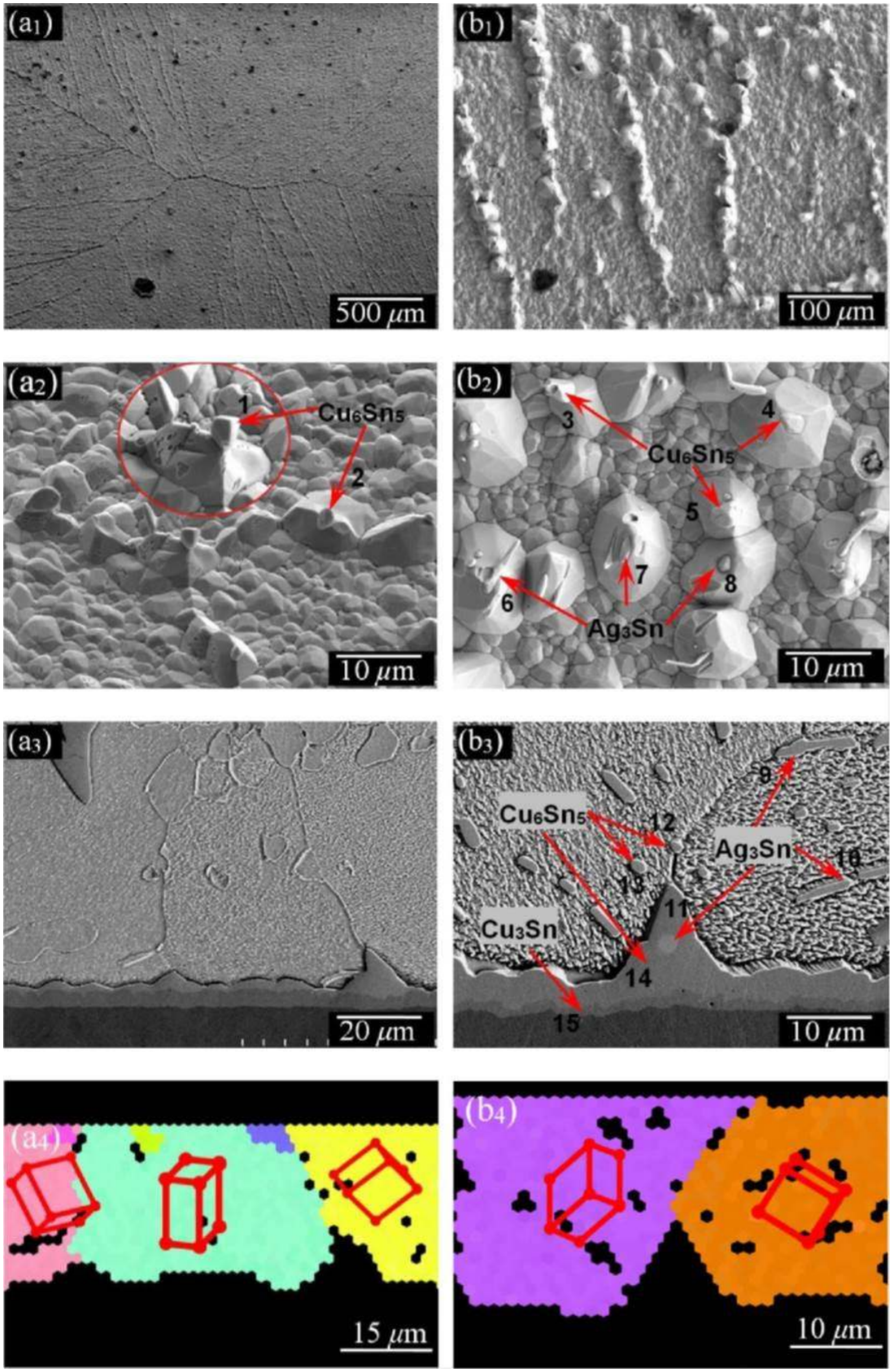

Figure 14: Representative SEM and EBSD images showing the abnormal growth of Cu_6Sn_5 grains formed at the (a) Sn/Cu and (b) Sn3.5Ag/Cu interface after 16 and 36 days of aging, respectively [101].

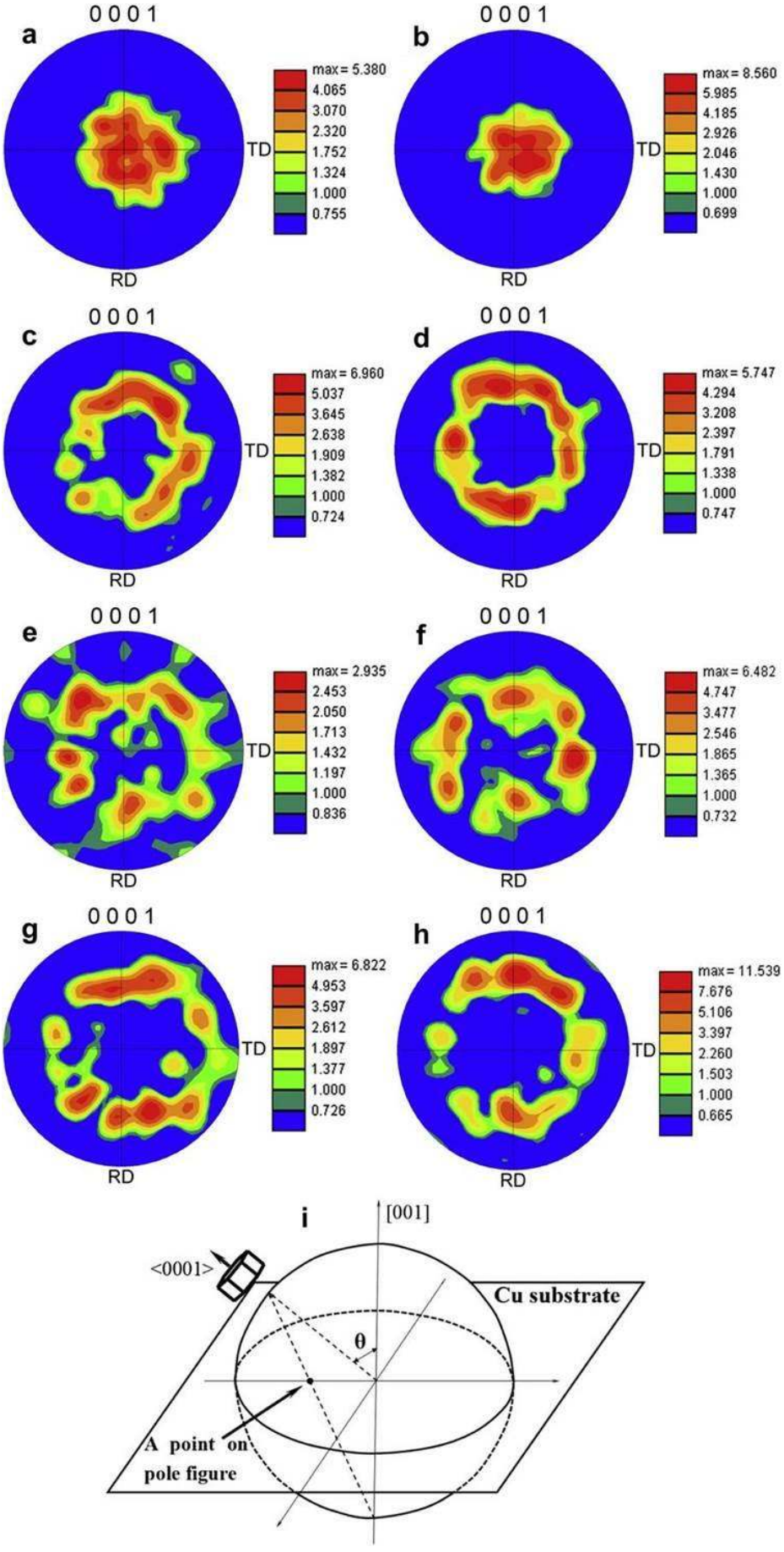

Figure 15: Pole figures of Cu_6Sn_5 formed at the (a-d) Sn3.5Ag/Cu and (e-h) Sn/Cu interfaces, and (i) diagram for Cu_6Sn_5 orientation. Reflow parameters are: (a, e) 240 ^oC, 30 min, (b, f) 240 ^oC, 600 min, (c, g) 280 ^oC, 30 min, and (d, h) 280 ^oC, 600 min [84].

Figure 16 : (a)Top-view scanning electron microscopy SEM image of Cu_6Sn_5 scallop-type grains on a Cu [128]; (b) Morphology of rooftop-type Cu_6Sn_5 formed on (100) Cu [128]; (c) on (111) Cu [129].

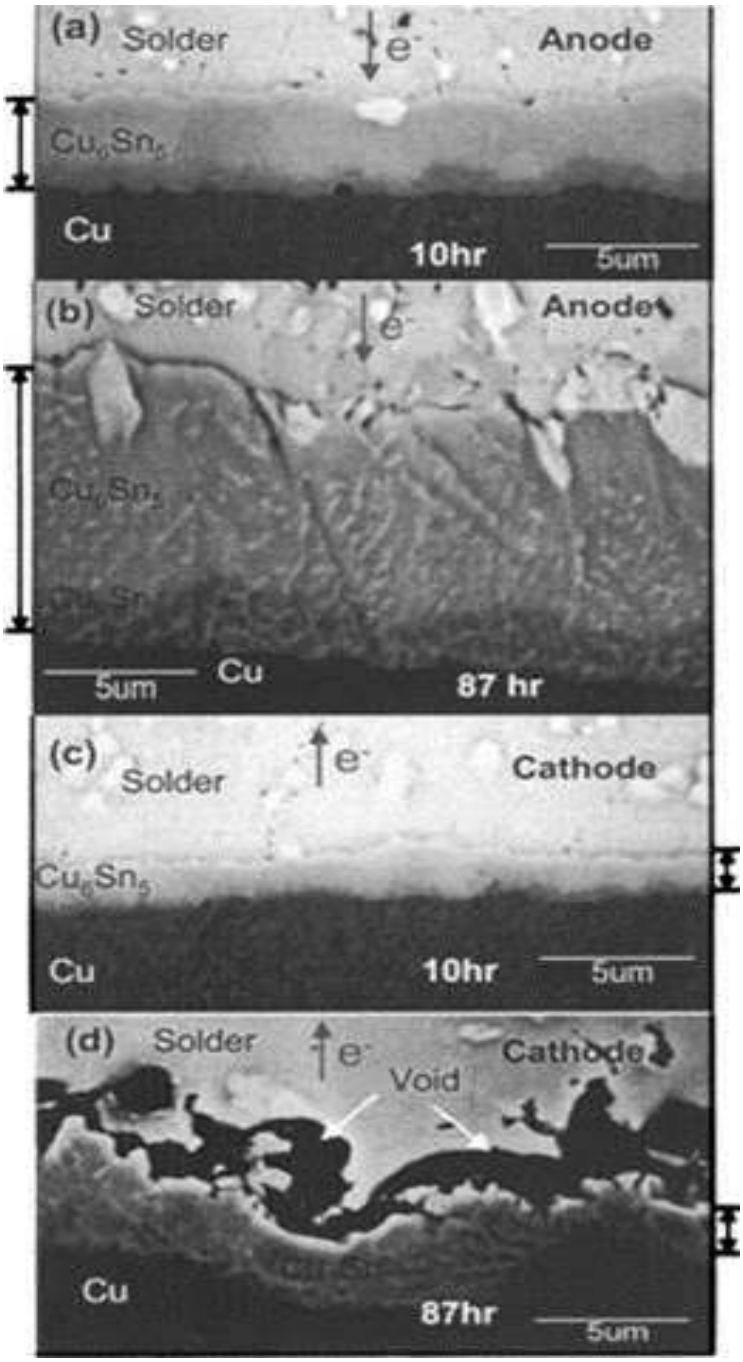

Figure 17: Scanning electron microscopy images of thickness change at the anode and the cathode, after current stressing of (a) 10 h (anode) (b) 87 h (anode), (c) 10 h (cathode), and (d) 87 h (cathode), with current density of 3.2×10^4 A/cm^2 at 180 °C [133].

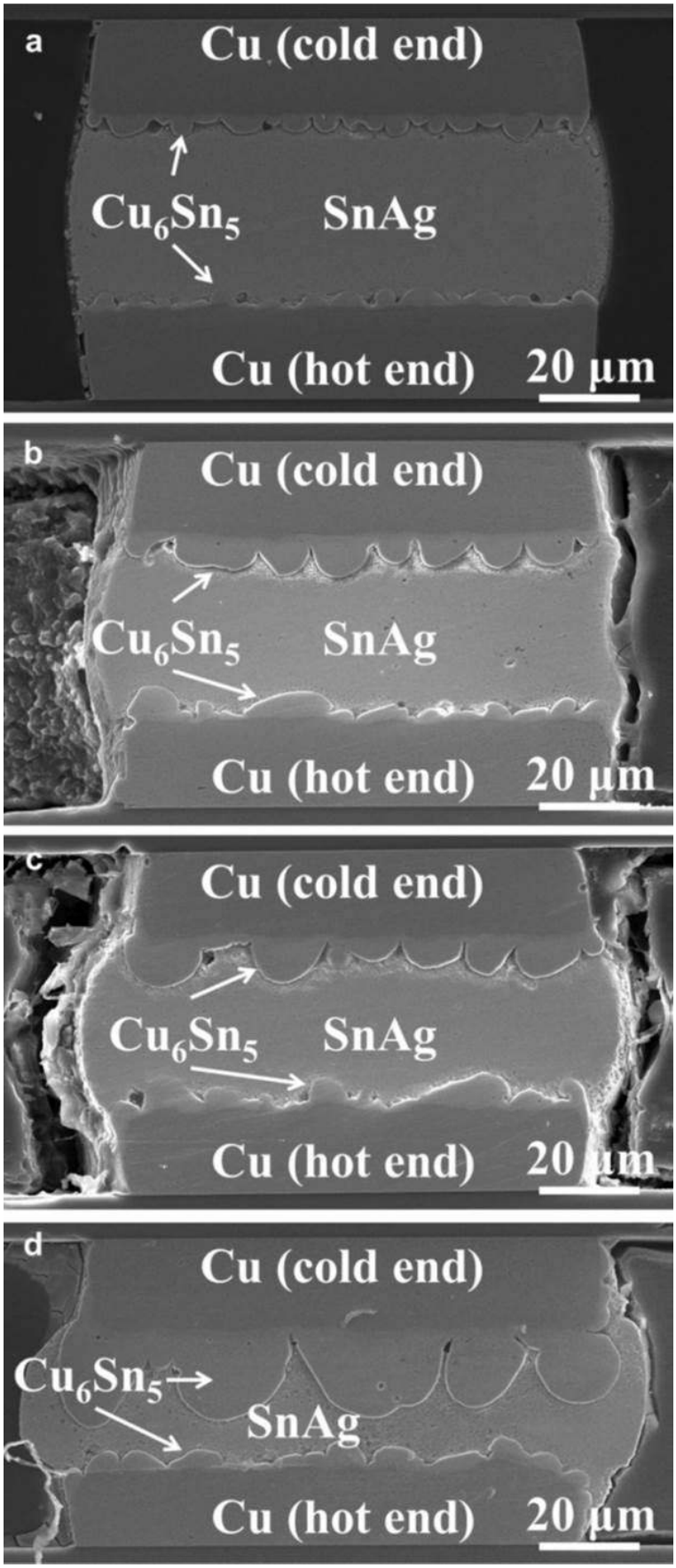

Figure 18: Cross-sectional SEM image of the flip-chip joints for (a) as-fabricated, (b) reflowed for 10 min, (c) reflowed for 20 min, (d) reflowed for 40 min at 260 °C on a hot plate. Asymmetrical growth of the interfacial became clearer as reflow time increased [134].

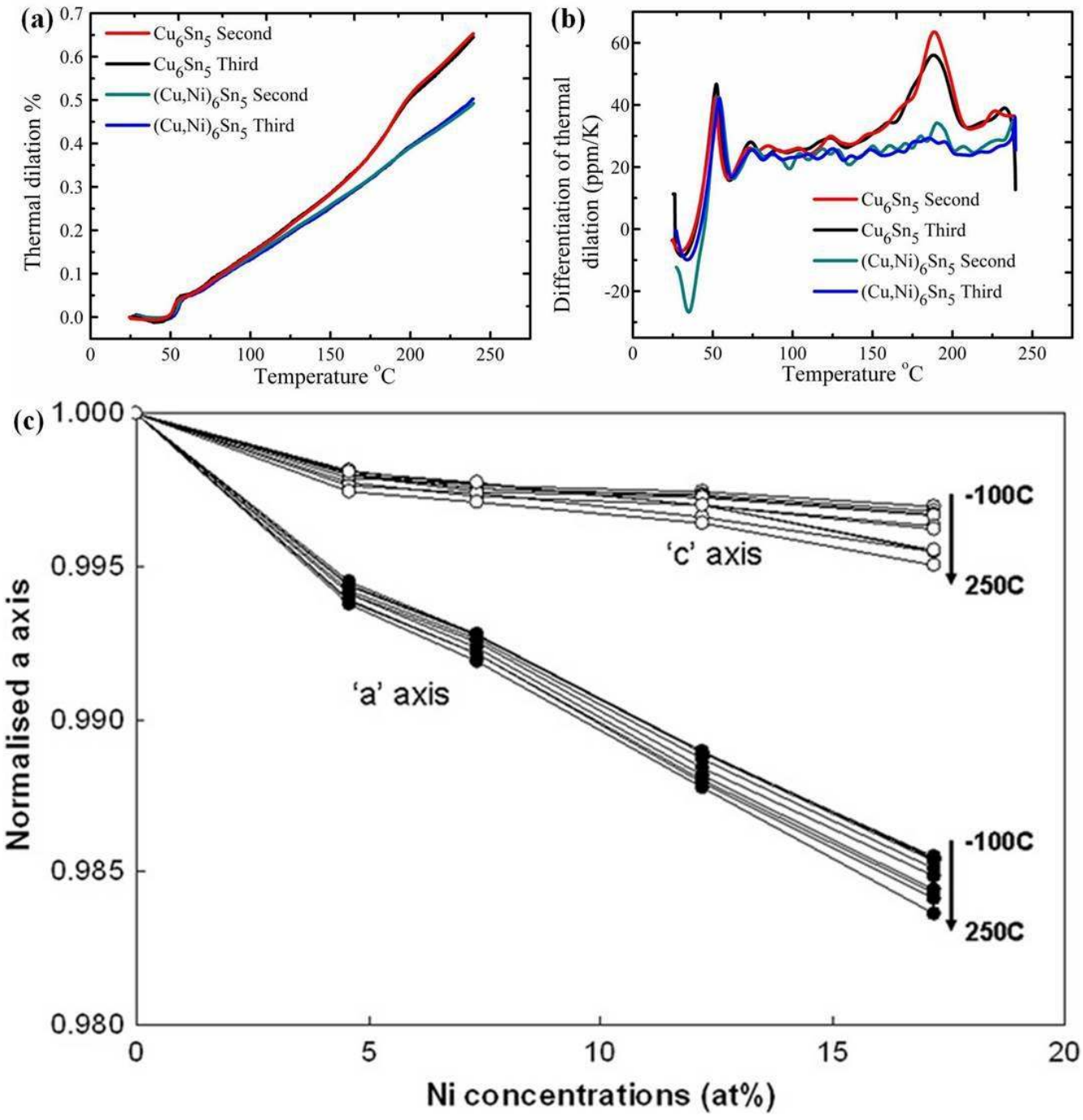

Figure 19: (a) Thermal dilation during heating stages [138], (b) differentiation of thermal dilation during heating stages [139], (c) Ni dependence of normalised a and c-axis of $Cu_{(6-X)}Ni_xSn_5$ (X= 0, 0.5,1,1.5 and 2) [139].

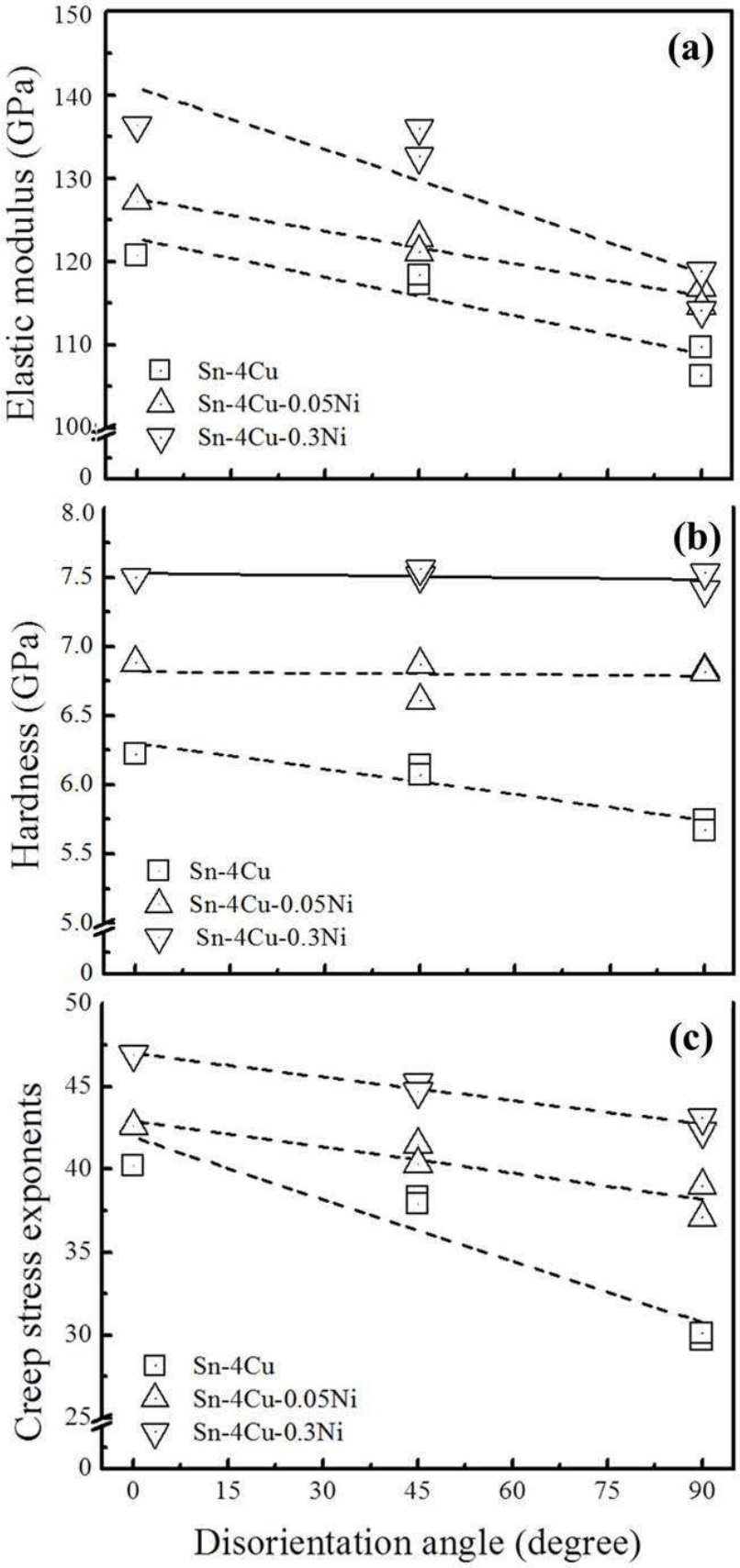

Figure 20**: Young's modulus of Cu_6Sn_5 grains as a function of θ (the angle between the orientation of grains and the c-axis of unit cell) [149].**

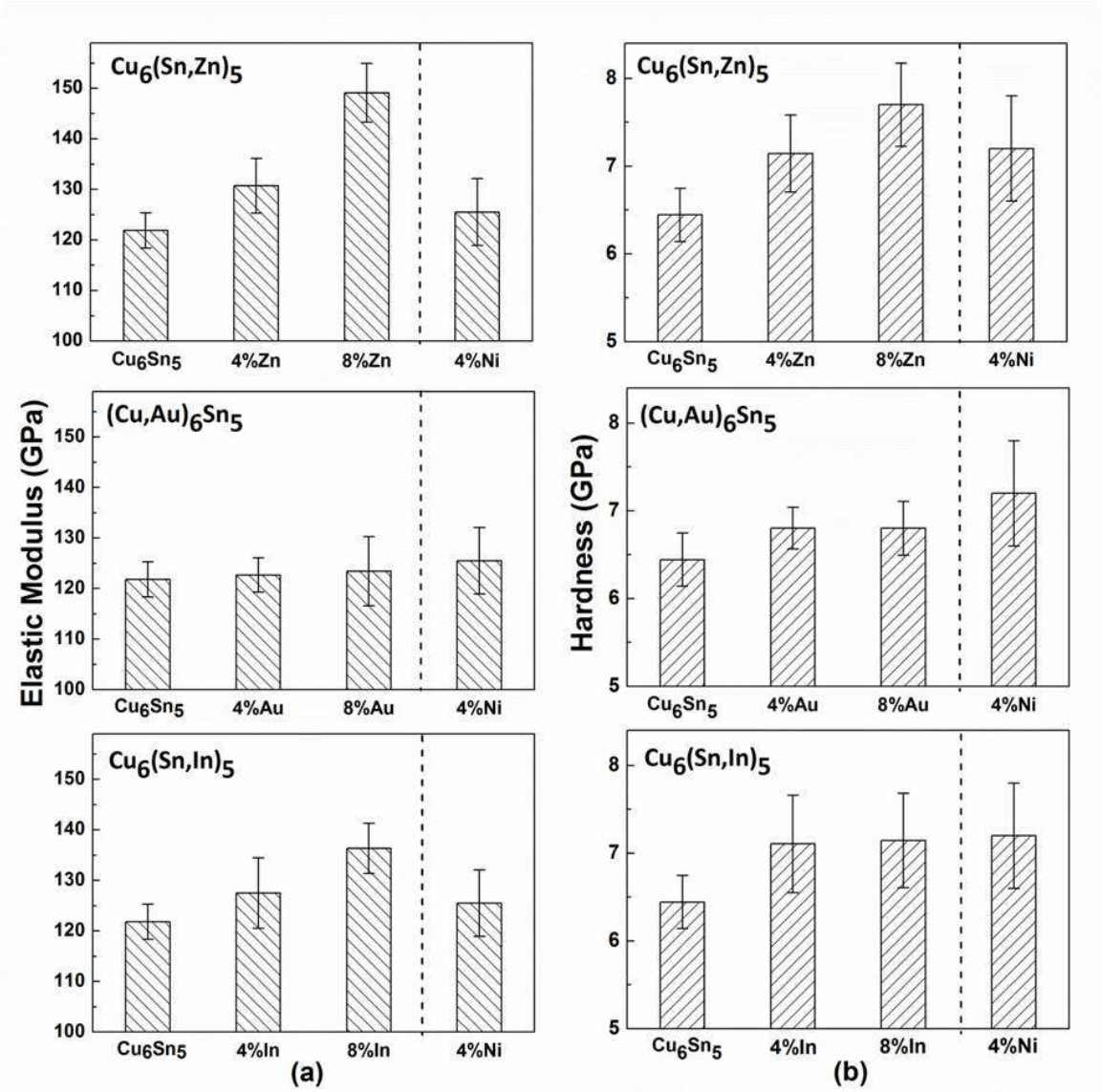

Figure 21: (a) elastic modulus and (b) hardness of Cu_6Sn_5 doped with Zn, Au and In [161].

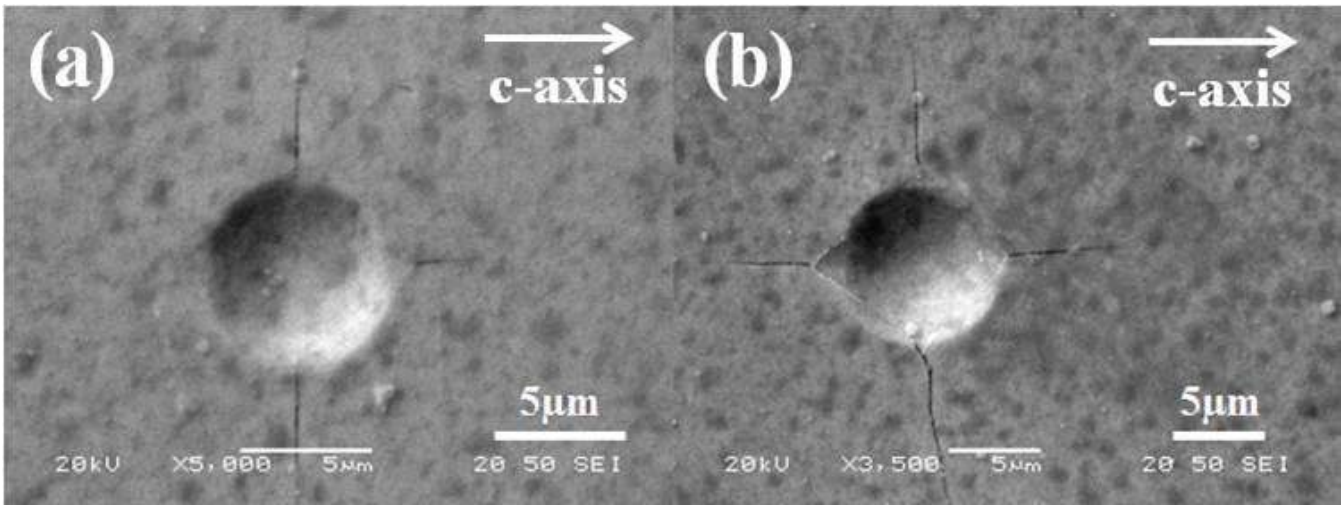

Figure 22: Crack pattern on crystal planes parallel to c-axis of Cu_6Sn_5 directionally solidified from Sn-4Cu alloys at (a) 30 and (b) 40 mN [149].

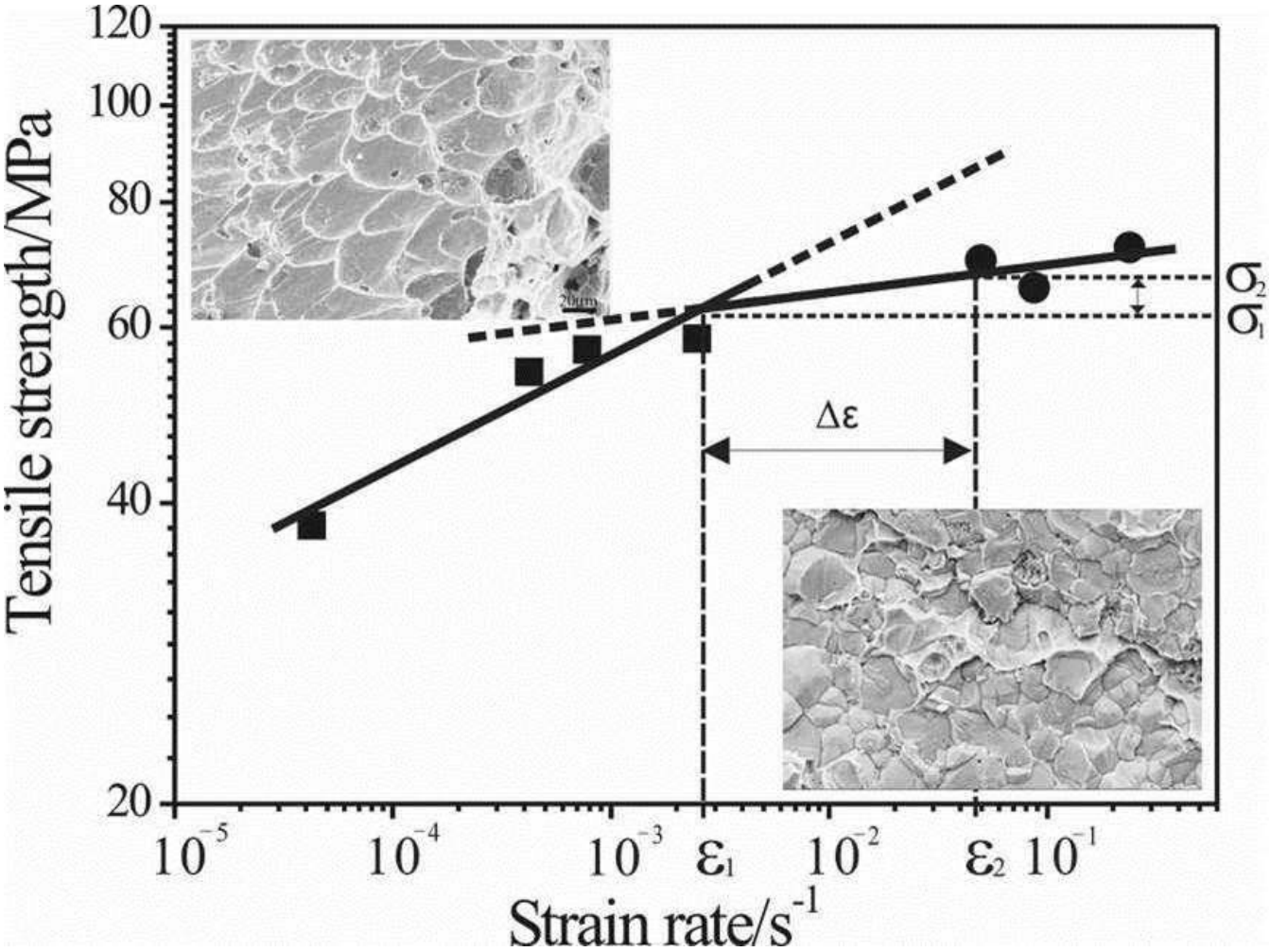

Figure 23: Plot of the lg σ_s − lg $\dot{\epsilon}$ curve of Sn–3Cu/Cu joint samples aging at 160 °C for 5 days [173].

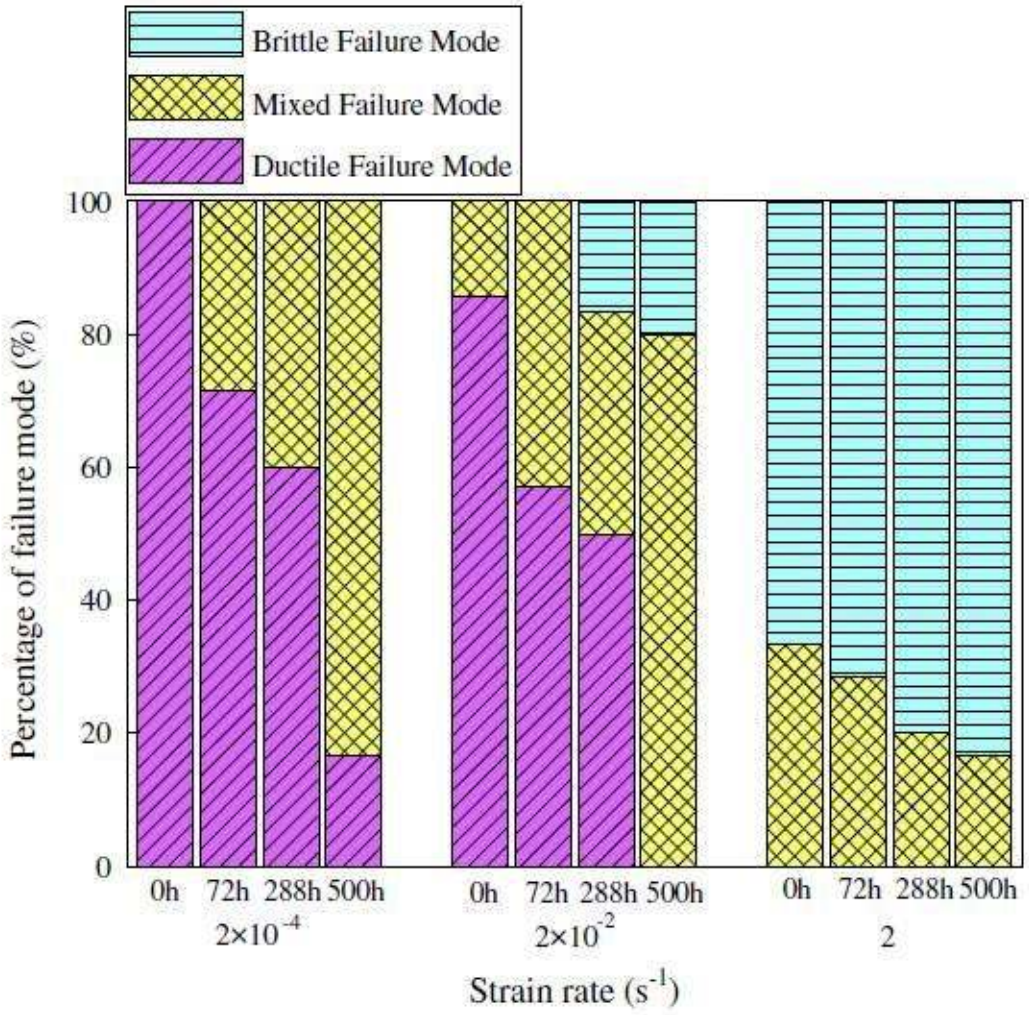

Figure 24: Distribution of the three failure modes occurred in the solder joints aged for different time and tested at different strain rates [180].

Table

Table1: Reported Crystal structures of Cu_6Sn_5

Phase	Structure	a (Å)	b (Å)	c (Å)	α	β	γ
η-Cu_6Sn_5 [16]	Hexagonal	4.190	b=a	5.086	90°	β=α	120°
η'-Cu_6Sn_5 [16]	Monoclinic	11.022	7.282	9.827	90°	98.84°	γ=α
η^6-Cu_6Sn_5 [8]	Monoclinic	12.60	7.27	10.20	90°	90°	γ=α
η^8-Cu_6Sn_5 [8]	Monoclinic	9.83	7.27	c=a	90°	62.5	γ=α
η^{4+1}-Cu_6Sn_5 [19]	Monoclinic	92.241	7.311	9.880	90°	118.95°	γ=α

Table 2: Elastic modulus and hardness of Cu_6Sn_5 at room temperature

IMCs	Young's modulus (GPa)	Hardness (GPa)	Reference
Cu_6Sn_5	91.7	3.6	[166]
	134±7	6.5±0.3	[187]
	144.9±1.5 to 125.0±6.8	5.62±0.35 to 6.27±0.30	[188]
	116.77±1.64	5.40±0.69	[141]
	59.0 to 115.1	2.44 to 6.67	[142]
	116.89±2.04 118.97 ± 1.93	6.35±0.20 6.45 ± 0.14	[143]
	112.3 ± 5.0	6.38 ± 0.21	[144] [10]
	124.16 to 129.38	7.31 to 6.84	[145]
	95.7 to 97.4	5.67 to 6.09	[146, 154]
	129.0± 4.0 to 133.9 ± 9.0	5.6± 2.1 to 4.8±1.9	[147]
	126.995±2.342 to 125.845±3.045 114.527±5.189 to125.845±3.045	6.47±0.156 to 6.824±0.104 6.222±0.08 to 6.749±0.147	[148]
	120.98±2.46 105.00±1.80	6.02±0.20 to 5.69±0.14	[150]
	115.5±4.1	n.a.	[169]
	130±9	6.67±0.43	[152]
	117±5	6.7±0.4	[153]
	126±2.4	7.24±0.09	[165]
	120	n.a.	[162]
	125.98	n.a.	[163, 189]
	93	n.a.	[137]